

LWIR spectroscopy on  
feldspars from rock plugs for  
the detection of permeable  
zones in geothermal systems.

DOREEN NYAHUCHO

July, 2020

SUPERVISORS:

Dr. C.A, Hecker

Dr. H.M.A, van der Werff





# LWIR spectroscopy on feldspars from rock plugs for the detection of permeable zones in geothermal systems.

DOREEN NYAHUCHO

Enschede, The Netherlands, July, 2020

Thesis submitted to the Faculty of Geo-Information Science and Earth Observation of the University of Twente in partial fulfilment of the requirements for the degree of Master of Science in Geo-information Science and Earth Observation.

Specialization: Applied Remote Sensing for Earth Sciences

SUPERVISORS:

Dr. Chris Hecker

Dr. Harald van der Werff

THESIS ASSESSMENT BOARD:

Prof. Cees van Westen (Chair)

Dr. Martin Schodlok, BGR Germany (External Examiner)

#### DISCLAIMER

This document describes work undertaken as part of a programme of study at the Faculty of Geo-Information Science and Earth Observation of the University of Twente. All views and opinions expressed therein remain the sole responsibility of the author, and do not necessarily represent those of the Faculty.

## ABSTRACT

Hydrothermal minerals indicate inferred permeability in geothermal systems besides being indicative of formation temperature, fluid composition and host rock composition. Minerals, particularly hydrothermal feldspars (adularia and albite), are important minerals in permeability studies. Adularia has a direct link to highly permeable zones, whereas albite is indicative of inferred low permeability. The ability to recognize and distinguish adularia from other feldspar minerals is, therefore, crucial. Spectroscopy has been used as an alternative approach relative to convectional methods to study feldspars minerals. However, there are limited spectroscopy studies on adularia, this study explores LWIR spectroscopy on rock plugs from the Karangahake epithermal Ag-Au system to map adularia and other associated minerals. These samples are used in the development studies of geothermal systems because the epithermal systems are fossil equivalents of geothermal systems, particularly low sulphidation systems, which are mainly found in highly permeable zones. The objective is to (1) understand spectral characteristics of feldspars; adularia and other hydrothermal minerals associated with it, (2) assess the performance of LWIR in the mapping of feldspar minerals and, (3) establish mineral assemblage that can be used to identify adularia-rich areas for permeability studies in the future.

A total of 50 hyperspectral images of 50 rock plugs of approximately 1inch diameter were acquired in the LWIR wavelength range by a hyperspectral imaging system. After processing of the acquired images for noise reduction and reflectance to emissivity conversion, wavelength mapping and Principal Component Analysis (PCA) algorithms were applied to facilitate endmembers collection. Once the endmembers were collected, they were compared to reference spectral libraries for mineral identification and naming. Then, the Spectral Angle Mapper (SAM) was used to classify and quantify the images based on the most dominant mineral per pixel. Also, Iterative Spectral Mixture Analysis (ISMA) algorithm was used to obtain fractional abundances of constituent mineral per pixel for easy comparison with TIMA data. Given unrealistic ISMA results, i.e., negative fractional abundance values, it was difficult to quantify the sample images for comparative analysis. Therefore, mineral quantification was done based on SAM classification results and ISMA provided an alternative approach to understand the spectral behavior of mixed pixels. Validation of the LWIR identified minerals was done using XRD measurements and TIMA data on the selected 35 samples.

Results present various feldspar minerals characterized by broad spectral features within 8100-10000nm spectral range. Other identified minerals are silica, carbonate and clay minerals. Spectral differences in wavelength position and shape (defined by width, depth and symmetry) of the diagnostic features reflect variability in their mineralogical composition and can be used to distinguish the identified minerals. LWIR mineral estimates indicate that rock samples have been altered to a certain extent due to the presence of alteration minerals such as adularia, albite, pyrite and calcite. The Identified minerals were common in all datasets; LWIR, TIMA and XRD data. This is despite the shortcomings in mineral mapping, such as

misrepresentation of minerals in LWIR maps. Generally, LWIR data were correlated to TIMA and XRD data by up to  $\sim 0.5$  correlation coefficient. The relationship between albite and adularia maintains its inverse relationship, suggesting the possibility of using this relationship in permeability studies. Hydrothermal minerals that commonly occur with adularia are quartz, calcite, albite and pyrite; however, this is insufficient to establish mineral assemblage for the identification of adularia-rich areas.

**Keywords:** LWIR imaging spectroscopy, hydrothermal minerals, adularia, inferred permeability, geothermal systems.

## ACKNOWLEDGEMENTS

First and foremost, I would like to extend my appreciation to the Netherlands Initiative for Capacity Building in Higher Education (NICHE) for their financial support throughout my two years of study. This scholarship was awarded to me through Tanzania-Dutch Energy Capacity Building (TDECB) program, jointly coordinated by the University of Dar Es Salaam (Tanzania) and the University of Twente (the Netherlands).

Much appreciation to the academic and non-academic staff of the department of Earth System Analysis (ESA), Faculty of Geo-Information Science and Earth Observation (ITC) of the University of Twente (UT) for their support throughout my two years of study.

I am forever grateful to my supervisors, Dr. Chris Hecker and Dr. Harald van der Werff, for their insightful comments, guidance, and commitment during my thesis. It was a great honor working under their supervision.

Special thanks to Mark Simpson and the University of Auckland for the materials used in this research, including rock samples, TIMA, and XRD data.

I also appreciate Prof Dr. Mark van der Meijde, for his comments and suggestions during the proposal and mid-term assessment presentation.

I acknowledge the Federal Institute for Geosciences and Natural Resources (BGR) in Hannover, Germany, for allowing us to use their laboratory facilities. Many thanks to Dr. Martin Schodlok and Chris Hecker for their assistance during image acquisition.

I would also like to thank Dr. Derek Rogge for the ISMA algorithm, Dr. Steven Ruff, for the chalcedony spectrum from his private spectral collection.

Last but not least, I would like to extend my gratitude to my family and friends for their moral support throughout the academic years.

# TABLE OF CONTENTS

---

1. INTRODUCTION .....	1
1.1. Background and Justification .....	1
1.2. Research Objectives .....	4
1.2.1. Main objective .....	4
1.2.2. Specific objectives .....	4
1.3. Research questions .....	4
1.4. Feldspar minerals .....	5
1.5. Spectral characteristics of feldspar minerals .....	6
1.6. Thesis structure .....	8
2. DATA AND METHODS .....	9
2.1. Dataset .....	9
2.1.1. Rock samples .....	9
2.1.2. XRD data .....	10
2.1.3. TIMA images (PNG) .....	10
2.2. Methods .....	10
2.2.1. TIMA (PNG) image processing .....	11
2.2.2. Hyperspectral image (HSI) acquisition .....	12
2.2.3. Hyperspectral Image pre-processing .....	13
2.2.4. Principal component analysis (PCA) .....	14
2.2.5. Wavelength mapping .....	14
2.2.6. Endmember extraction and Identification .....	15
2.2.7. Spectral Angle Mapper (SAM) .....	16
2.2.8. LWIR-TIMA-XRD comparative analysis .....	17
2.2.9. Establishing mineral assemblage for adularia-rich areas .....	18
3. RESULTS .....	19
3.1. Image pre-processing results .....	19
3.2. Principal Component Analysis (PCA) results .....	20
3.3. Wavelength Map .....	21
3.4. Endmembers .....	22
3.4.1. Feldspar minerals .....	23
3.4.2. Other associated minerals .....	25
3.5. Mineral mapping results .....	27
3.5.1. SAM classification results .....	27
3.5.2. ISMA results .....	29
3.6. Comparative analysis .....	31
3.6.1. Visual comparison: HIS and TIMA .....	31

3.6.2. Quantitative comparison: HSI, TIMA and XRD .....	33
3.7. Association of adularia with other minerals .....	35
4. DISCUSSION.....	37
4.1. Methods .....	37
4.2. Spectral characteristics of feldspars and other minerals.....	38
4.3. LWIR mapping of feldspars and associated minerals.....	40
4.4. Hydrothermal alteration.....	42
5. CONCLUSION AND RECOMMENDATIONS .....	44
6. APPENDICES .....	50

# LIST OF FIGURES

---

Figure 1.1: Feldspar classification diagram, endmembers are in wt% (adapted from Kumar, Marcolli, & Peter, 2019).....	5
Figure 1.2: Emissivity spectra of potassium feldspars in LWIR region (arrows indicate emissivity minima).....	6
Figure 1.3: Emissivity spectra of anorthoclase in LWIR region (arrows indicate emissivity minima) .....	7
Figure 1.4: Emissivity spectra of plagioclase feldspars in LWIR region (arrows indicate emissivity minima) .....	7
Figure 2.1: Rock sample AU57545.....	9
Figure 2.2: An example of a TIMA mineral map (in PNG format) for sample AU57565 .....	10
Figure 2.3: Methodological flowchart .....	11
Figure 2.4: Rock samples on a wooden plank (a yellow arrow showing the scanning direction -top of the HSI) .....	12
Figure 3.1: a) MNF output bands and b) eigenvalue plot for sample AU57602.....	19
Figure 3.2: a) Reflectance spectra(offset for clarity) before (solid line) and after (dotted line) forward and backward MNF transformation b) emissivity spectrum after reflectance to emissivity conversion.....	20
Figure 3.3: Band combination RGB= PC135 and PC321 for sample AU57491(left) and AU57602(right) 20	
Figure 3.4: A wavelength map for AU57491 (left) and AU57602 (right).....	21
Figure 3.5: Spectra from wavelength maps of AU57491(left) and AU57602 (right) corresponding to colours highlighted in the maps in figure3.4 (Vertical lines show emissivity minima and arrows shows emissivity peaks) .....	21
Figure 3.6: Plagioclase spectra from LWIR images (black) versus reference spectra (red) from an existing spectral library.....	23
Figure 3.7: Alkali feldspar spectra from LWIR images (black) versus reference spectra from spectral libraries (red) .....	24
Figure 3.8: Spectra from LWIR images (black) compared with reference spectra from the existing spectral library (red).....	26
Figure 3.9: LWIR mineral maps for various rock samples .....	28
Figure 3.10: Spectra from AU57504 corresponding to unclassified pixel in the mineral map.....	28
Figure 3.11: Veins (~1mm width) in LWIR maps.....	28
Figure 3.12: Percentage estimates of quartz(inner circle) versus percentage estimates of Quartz+50% mineral mixtures of quartz (outer circle) .....	29
Figure 3.13: Abundance profile for fractional abundances per pixel (left) with their corresponding spectral signature (right). This is for the pixel where ISMA worked.....	30
Figure 3.14: Abundance plots (left) of one of the problematic pixel with its corresponding rms profile (right).....	30

Figure 3.15: Comparison of the spatial distribution of minerals between wavelength maps, SAM classified images and TIMA maps for sample image AU57493, AU57522, AU57540 and AU57510 ..... 31

Figure 3.16: a) SAM classified image(right) and ISMA results for sample AU57545 b) their corresponding spectra (right) and abundance profile(left) ..... 32

Figure 3.17: Cross plots of HSI(LWIR) versus TIMA and XRD mineral percentage estimates for adularia, albite quartz and calcite..... 34

Figure 3.18: Adularia versus albite occurrence in the decreasing order of adularia content (to the right)... 35

## LIST OF TABLES

---

Table 2.1: Specification for an OWL 3 imaging system.....	12
Table 2.2: Parameters for ISMA tool.....	17
Table 3.1: Description of the 12 selected endmembers.....	23
Table 3.2: Mineral abundance for few sample images.....	27
Table 3.3: Unmixing results for sample image AU57535.....	29
Table 3.4: LWIR mineral percentage estimates for the ten selected adularia-rich samples with >30% adularia.....	35
Table 3.5: Common minerals associated with the occurrence of adularia from LWIR classified results.....	36

## LIST OF APPENDICES

---

Appendix 1: SAM classified Images.....	50
Appendix 2: Mineral estimates for LWIR maps.....	51
Appendix 3: TIMA mineral percentage estimates.....	52
Appendix 4: XRD mineral percentage estimates.....	53
Appendix 5: Image acquisition log file.....	53



# 1. INTRODUCTION

## 1.1. Background and Justification

Geothermal energy is clean, renewable energy with little or no carbon dioxide emission (Lin & Zhu, 2019). Its resources are found within the earth's crust at depths of approximately >1km and only found at a depth of 4-5km under pressured reservoir conditions (van der Meer et al., 2014). The heat extracted from the geothermal reservoir is for several economic uses depending on reservoir temperature conditions that are influenced by circulating thermal fluids (Hochstein, 1988). High-temperature resources (>125°C) are mostly used for electricity generation while low temperatures (<125°C) are for direct utilization of heat in industries, homes, etc. (Hochstein, 1990). Due to the high demand for such clean energy, more emphasis has been put on various methods for geothermal energy exploration and production (Kerr, 2017).

Geothermal energy production highly depend on rock permeability, which indicate the capacity of the rock in transmitting fluids (Browne, 1970). Several methods have been used over time to estimate permeability and identify permeable zones. Such methods are, for example, geophysical logging and well permeability test (Baptiste & Chapuis, 2015; Field, Rafik, & Kamel, 2017). These methods require lengthy site preparation, which includes drilling of the well for them to be performed. Prior to the application of such methods, mineral assemblage and alterations have been used as indicators for temperature and permeability in early stages of exploration and production of geothermal energy.

Mineral alterations can be of hydrothermal or non-hydrothermal origin. Hydrothermal minerals form as a result of an interaction between hot circulating fluids and host rock (Pirajno, 2010). Nature of their occurrence differs based on variation in temperature, fluid composition, host rock composition and permeability (Yang, Huntington, & Browne, 2000). Minerals such as quartz, chlorite, calcite, pyrite and clays are known to be temperature indicators due to their stability at specific temperature conditions (Simmons & Browne, 2000). Pyrrhotite, pyrite and feldspars are known to be indicative of impermeable and permeable zones due to specific occurrence conditions.

Feldspars (plagioclase and K-feldspars) are the most common rock-forming minerals with varying structural and chemical composition. Hydrothermal feldspars such as adularia and albite form as a replacement or depositional minerals at different temperature and pressure conditions. The formation of, for example, adularia (K-feldspar) relates to the boiling zone, which is associated with permeable zones. This association has been consistent in previous geothermal studies and led to the assumption that adularia can potentially be indicative of high permeability in geothermal systems (Browne & Ellis, 1970; Simmons & Browne, 2000).

As reported by Browne, (1970), the occurrence of hydrothermal altered feldspars, adularia and albite relate to high and low permeability zones, respectively. Similarly, observations made by Bogie & Lawless, (2000) shows the dominance of adularia in productive zones compared to albite. However, there is a lack of conclusive explanation on the level of permeability when adularia and albite coexist (Browne & Ellis, 1970; Simpson et al., 2019). To better understand different permeability levels where both adularia and albite exist, identification, quantification and determination of the spatial distribution of adularia and albite is of importance for future permeability studies within geothermal systems.

Several methods have been extensively employed to study feldspar minerals, i.e., identify various members of the feldspar mineral group. Such methods include conventional methods; visual inspection, X-ray and petrographic analysis. Interpretation by visual inspection can have a user bias and highly depend on the knowledge of the interpreter. X-ray analysis includes XRF (X-ray fluorescence) and XRD (X-ray diffraction) techniques. XRF and XRD quantitatively determine the elemental and mineralogical composition of a rock, respectively (Černý & Chapman, 1984; Nijenhuis, Gataeshki, & Fransen, 2009). These methods have been used despite their limitation to the determination of the spatial distribution of minerals. Petrographic analysis has also been useful in distinguishing feldspars based on differences in crystal structures and appearance under the microscope.

Recently, another automated mineral mapping method, TIMA (TESCAN Integrated Mineral Analyzer), has demonstrated to be significant in mapping feldspar minerals. This method uses the latest developments of automated mineralogy (AM) systems, which allow detailed data collection with a high spatial resolution of up to approximately 2 $\mu$ m (Hrstka, Gottlieb, Skála, Breiter, & Motl, 2018). This level of detail was not possible to obtain through human-interactive operation of SEM/EDX system. However, mineral identification, mineral quantification and determination of their spatial association are limited to mixed pixels and very fine mineral grains (Simpson et al., 2019).

Infrared spectroscopy is another alternative method for mineral mapping in the wavelength region of VNIR (visible-near infrared), SWIR (shortwave infrared) and LWIR (longwave infrared) (Hecker, der Meijde, & van der Meer, 2010). For rock-forming minerals, LWIR imaging is ideal for semi-quantification and spatial distribution determination. This is possible due to varying composition and structural state of minerals, which result in unique spectral signatures. The spectral signatures of feldspars are characterized by reststrahlen features in the LWIR region (Riley & Hecker, 2013). These diagnostics features are pronounced at around 8000-14000nm as a result of vibrational processes within the structural framework of feldspar minerals (Hunt, 1977).

LWIR spectroscopy of feldspars has been documented since the 1950s. Reflectance and emission infrared spectroscopy are the most preferred spectroscopy techniques, ideal for comparison studies with remote

sensing data (Hecker et al., 2010). Studies were done using this technique to understand the spectral behavior of feldspars. For example, Feely & Christensen, (1997) used LWIR spectroscopy to map feldspars as a group of minerals in igneous and metamorphic petrology. These mineral groups, alkali feldspars and plagioclase, were useful in rock classification (Graham R. Hunt & John W. Salisbury, 1970).

Nevertheless, few studies have attempted to map various members of the feldspar mineral group using LWIR spectroscopy, for example, in Ruff, (1998); Christensen et al., (2000); Hecker & Dilles, (2012). Such minerals are albite, oligoclase, orthoclase and labradorite. Results have demonstrated LWIR spectroscopy as a potential tool in distinguishing some of the potassic, sodic and calcic endmembers of feldspars. This was demonstrated in a study by Hecker et al., (2010), showing distinctive reststrahlen features for albite that are distinguishable from other feldspar minerals.

However, limited studies have specifically investigated LWIR spectroscopy of adularia and its discrimination from other feldspars. Investigated feldspar minerals, for example, adularia and orthoclase, appear to have almost similar spectral signatures except for minor variations in the intensity and wavelength position of the diagnostic features (Reitze et al., 2019). Given the nature of feldspar samples used in Reitze et al., (2019), mixed mineral composition made the distinction of adularia from other feldspars difficult.

Therefore, this study investigate the possibility of distinguishing adularia from other feldspar minerals using LWIR imaging spectroscopy. The scope of the study is limited to available rock samples that were acquired from a low sulfidation epithermal gold system, which is known to be a fossil equivalent of a geothermal system. These rock samples were also used in the study of Simpson et al. (2019). LWIR imaging spectroscopy is used to identify and quantify feldspar and other associated minerals. The results are compared to previously published TIMA and XRD results of the same rock samples. The comparison aims at assessing the performance of LWIR in the detection of various members of the feldspar mineral group. Finally, the results will suggest whether adularia, albite, and other feldspars can be distinguished by LWIR imaging spectroscopy. In Addition, information gained can then be used to understand permeability in active geothermal systems in the future.

## **1.2. Research Objectives**

### **1.2.1. Main objective**

The objective is to determine whether LWIR spectroscopy can reliably distinguish adularia from albite and other feldspars and work as a permeability indicator in geothermal systems in the future.

### **1.2.2. Specific objectives**

1. To understand spectral characteristics of feldspar minerals present in the low sulfidation epithermal gold system dataset using LWIR imaging spectroscopy.
2. To assess the capabilities of LWIR imaging spectroscopy in distinguishing adularia from other feldspar minerals.
3. To establish mineral assemblages that can be used to identify adularia-rich areas.

## **1.3. Research questions**

1. Which feldspar minerals can be identified by LWIR imaging spectroscopy in the investigated dataset?
2. Which minerals can spectrally be confused with adularia?
3. Which other hydrothermal minerals are spatially associated with adularia?
4. How well does the spatial distribution of minerals in LWIR mineral maps resemble those in TIMA mineral maps?
5. How well can LWIR quantify feldspars and other associated minerals compare to TIMA and XRD data? Is it possible to distinguish adularia from other feldspar minerals using the LWIR techniques?

#### 1.4. Feldspar minerals

Feldspars are a group of rock-forming aluminosilicate minerals that contain potassium [ $\text{KAlSi}_3\text{O}_8$ ], sodium [ $\text{NaAlSi}_3\text{O}_8$ ], or calcium [ $\text{CaAl}_2\text{Si}_2\text{O}_8$ ]. They occur in various rock types from igneous rocks through magma crystallization, metamorphic and sedimentary rocks (Dietrich, 2018). The identification of feldspars is based on the composition and arrangement of their constituent atoms and ions and therefore categorized into two groups, the alkali feldspars and plagioclase feldspars.

The alkali feldspars vary in composition between sodium aluminosilicate [ $\text{NaAlSi}_3\text{O}_8$ ] and potassium aluminosilicate [ $\text{KAlSi}_3\text{O}_8$ ]. They include sanidine, microcline, anorthoclase, orthoclase and perthite. Based on their temperature of formation, sanidine and anorthoclase are stable at high temperatures while adularia and perthite are known as low-temperature forms. Adularia, a low-temperature variety of orthoclase or microcline, contain  $\sim 90\text{wt}\%$   $\text{KAlSi}_3\text{O}_8$  (Reitze et al., 2019). Adularia commonly occurs in the hydrothermal environment and has been documented as a common alteration mineral, indicative of permeable zones/structures in geothermal systems.

The plagioclase feldspars vary in composition between sodium aluminosilicate [ $\text{NaAlSi}_3\text{O}_8$ ] and calcium aluminosilicate [ $\text{CaAl}_2\text{Si}_2\text{O}_8$ ]. They include albite, andesine, oligoclase, anorthite, labradorite and bytownite. Figure 1.1 demonstrates various feldspar minerals based on their composition, which varies in mineral percentages of calcium, sodium and potassium. As indicated in the figure below, for example, for anorthoclase,  $\text{Ab}_{10-37}$  indicates that anorthoclase is composed of 10-37 wt%  $\text{KAlSi}_3\text{O}_8$  and the rest is wt%  $\text{NaAlSi}_3\text{O}_8$ .

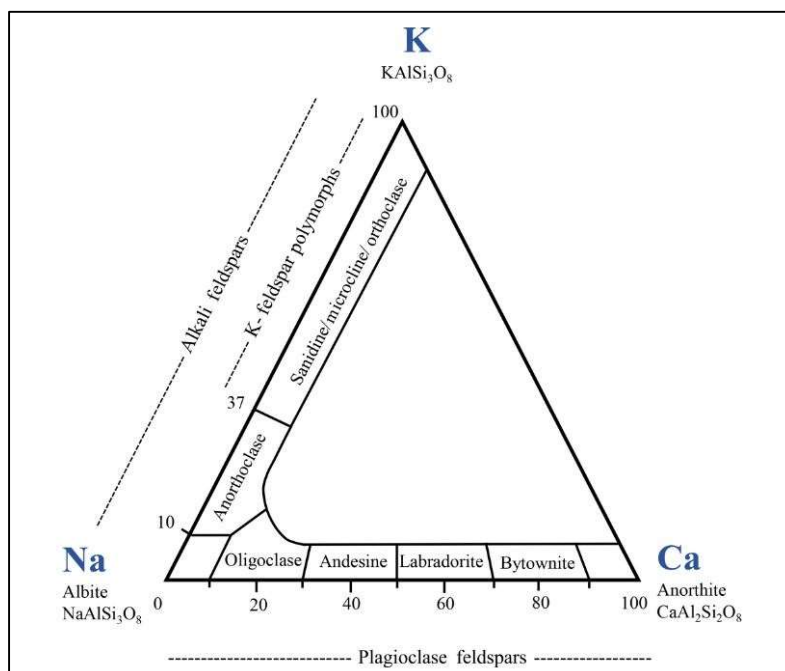


Figure 1.1: Feldspar classification diagram, endmembers are in wt% (adapted from Kumar, Marcolli, & Peter, 2019)

## 1.5. Spectral characteristics of feldspar minerals

Spectroscopy is useful in the identification and differentiation of minerals of hydrothermal and non-hydrothermal origin due to their spectral responses. Spectroscopy measures and analyzes spectra that result from the interaction between electromagnetic radiation and rock samples. Spectral characteristics of such minerals, particularly feldspars, vary in terms of band position and shape of the spectral features reflecting their composition and structural arrangement of their constituent ions. These features are due to asymmetric Si-O-Si stretching vibrations and Si-O-Al vibrations as documented by Salisbury, Walter, Vergo, & D'Aria, (1991). A detailed description of the vibrational processes in minerals and their signatures in the LWIR region referred to as Mid-Infrared region are presented in studies by Thomson & Salisbury, 1993; Christensen et al., 2000; Hunt, 1977.

Generally, feldspar minerals exhibit major diagnostic features between 8000nm and 12000nm. However, secondary features beyond 12000nm are also useful in the identification and distinction of minerals, for example, albite from other feldspar minerals. Below are the spectral characteristics of previously investigated feldspar minerals. The spectral information presented here is obtained from the existing spectral library by United States Geological Survey (USGS)(Kokaly et al., 2017), Arizona State University (ASU)(Christensen et al., 2000), Johns Hopkins University (JHU) and Commonwealth Scientific and Industrial Research Organisation (CSIRO) (Schodlok, Green, & Huntington, 2016) as implemented in The Spectral Geologist (TSG) version 8.

### Potassium feldspar

Adularia [ $KAlSi_3O_8$ ] has diagnostic features within 8400nm-10000nm due to molecular vibrations. Adularia displays two (in usgs) and three (in CSIRO) spectral features with their emissivity minima at ~8400nm and 9500-9600nm; ~8800, 9400 and 9600nm, respectively. Orthoclase [ $KAlSi_3O_8$ ] displays two spectral emissivity minima at ~8400nm and 9600nm. Microcline [ $KAlSi_3O_8$ ] has four spectral features with their emissivity minima at ~8500nm, ~9100nm, 9400nm and 9800nm. The deepest feature varies between the 9400nm and 9800nm.

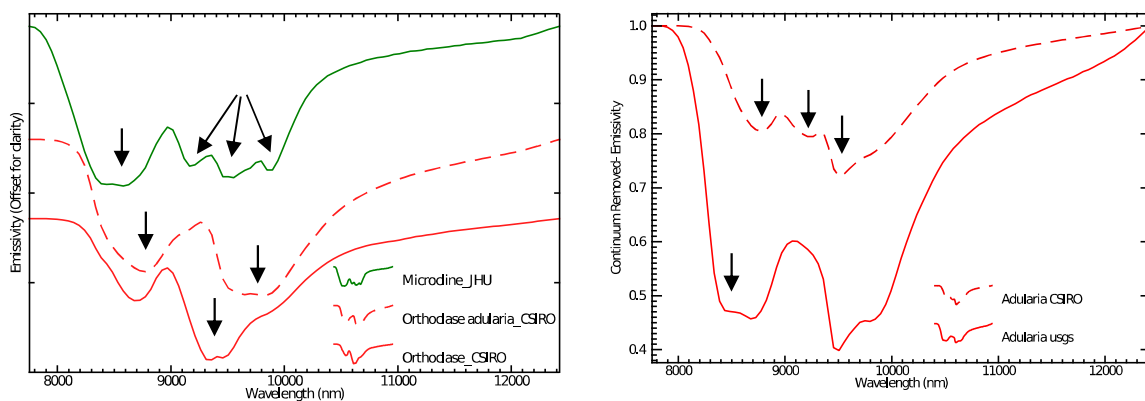


Figure 1.2: Emissivity spectra of potassium feldspars in LWIR region (arrows indicate emissivity minima)

Anorthoclase,  $(\text{Na},\text{K})\text{AlSi}_3\text{O}_8$  has spectral emissivity minima at  $\sim 8400\text{nm}$  and  $\sim 9600\text{nm}$ . The second feature appears deep compared to the first feature.

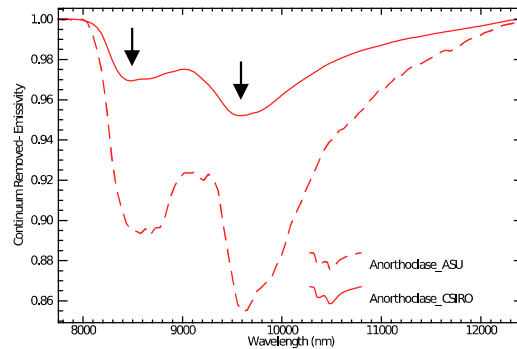


Figure 1.3: Emissivity spectra of anorthoclase in LWIR region (arrows indicate emissivity minima)

### Plagioclase feldspar

Albite,  $\text{NaAlSi}_3\text{O}_8$  is characterized by four spectral features. The first emissivity minima occur at  $\sim 8400\text{nm}$  and the second minima is at  $\sim 9200\text{nm}$ , followed by a doublet at  $\sim 9600\text{nm}$  and  $\sim 9900\text{nm}$ . The  $\sim 9600\text{nm}$  feature being the deepest feature. Also, albite has four weak absorptions at around  $13000\text{nm}$  which can be used to distinguish adularia from other feldspar minerals. When mixed with, for example, quartz, the second multiple features become less pronounced (Thomson & Salisbury, 1993). Oligoclase,  $(\text{Na},\text{Ca})[\text{Al}(\text{Si},\text{Al})\text{Si}_2\text{O}_8]$  displays spectral emissivity minima at  $8600\text{nm}$  and  $9600\text{nm}$ . The two features can form weak doublet features in some cases. Andesine,  $(\text{Na},\text{Ca})[\text{Al}(\text{Si},\text{Al})\text{Si}_2\text{O}_8]$  has two characteristic spectral features with their emissivity minima at  $\sim 8400\text{nm}$  and  $\sim 9600\text{nm}$  with a subtle feature at  $9900\text{nm}$ . The andesine spectrum resembles anorthoclase except for the additional feature at  $9900\text{nm}$ . The deepest feature in andesine occurs at  $\sim 9600\text{nm}$ , but when mixed with quartz, the presence of quartz might result in the  $\sim 8400\text{nm}$  or  $\sim 9200\text{nm}$  becoming the deepest feature. It also has three weak secondary features beyond  $12000\text{nm}$ .

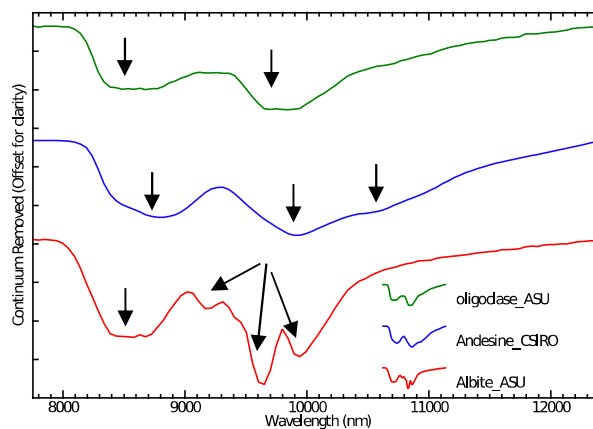


Figure 1.4: Emissivity spectra of plagioclase feldspars in LWIR region (arrows indicate emissivity minima)

## **1.6. Thesis structure**

This thesis is organized into five chapters. Chapter 1 introduces the research background and justification of the research problem, research objectives, research questions, theoretical background on feldspars, and LWIR spectral characteristics of feldspars. Chapter 2 presents datasets and methods, including image acquisition, image pre-processing, endmember extraction, mineral mapping, qualitative and quantitative comparison of LWIR, TIMA and XRD mineral abundances, analysis and interpretation. Chapter 3 presents the results of the image pre-processing and processing, qualitative and quantitative comparison of various datasets. Chapter 4 discusses the methods employed and results obtained from this research in comparison to the existing literature. Chapter 5 present a conclusion and recommendations.

## 2. DATA AND METHODS

Data used in this study include sample materials (rock samples) and supporting analytical data (TIMA and XRD) from a study by Simpson et al., (2019). The rock samples were used to acquire hyperspectral images using LWIR imaging spectroscopy. The acquired images were pre-processed and processed to extract spectral/mineralogical information. The processed images were then analyzed together with XRD and TIMA data of the same rock samples to assess the performance of LWIR imaging spectroscopy in identification and mapping of minerals present in the investigated dataset. Software used for data analysis are ENVI 5.5 + IDL 8.7, Hyppy3 and Excel. The sections below explain all methodological steps in detail.

### 2.1. Dataset

#### 2.1.1. Rock samples

A total of 50 rock samples collected from a low sulfidation gold system of Karangahake, New Zealand, were used. These samples are polished miniplugs of ~1inch (2.5cm) diameter labeled with code AU#, which stands for Auckland University (*figure2.1*). 13 samples of the 50 samples were collected from riversides and ridges (Keillors crosscut) and the rest were collected from surface outcrops.

The plugs were previously carbon coated for the study of Simpson et al., (2019). For this study, the carbon coat was removed by Chris Hecker at Remote Sensing and GIS (RSG) laboratory, ITC faculty, university of Twente. The procedure involves the use of a struers wet polishing machine with a fine Silicon Carbide Grinding Paper, Grit 4000 to grind and polish the rock surface for about 10-15 seconds per sample with about 10kg of pressure. The first three samples AU57540A, AU57540B and AU57577, were done longer. Therefore, there is a probability that surface material was grounded away for these particular samples. Then samples were rinsed with distilled water and dried in an oven for 48 hours at 50°C not to damage hydrated minerals such as zeolites. These procedures were personally communicated to me by Dr. Chris.

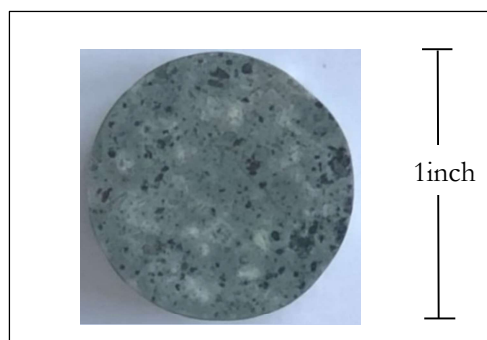


Figure 2.1: Rock sample AU57545

### 2.1.2. XRD data

X-ray diffraction (XRD) is an analytical technique used for the identification and quantification of crystalline minerals. As described by Simpson et al., (2019), homogeneous rock powders were scanned with a Philips PW 1050/25 diffractometer at the University of Auckland, New Zealand, to determine average bulk composition. One hundred nineteen samples were used and only 42 samples were selected for XRD and TIMA analysis. Therefore, XRD data available for this study are only for the selected 42 samples. These samples are among the 50 rock samples described in section 2.1.1. The mineral abundances calculated from 42 XRD scans are displayed in *appendix4*.

### 2.1.3. TIMA images (PNG)

A Tescan Integrated Mineral Analyzer (TIMA), also known as an automated mineral analyzer, is an analytical scanning electron microscope that measures modal abundance on multiple samples of grain mounts and thin or polished sections. TIMA was used to analyse the 42 polished samples at the Australian Resources Research Centre, Commonwealth Scientific and Industrial Research Organisation (CSIRO), Perth, Australia (Simpson et al., 2019). The rock samples were scanned at a spatial resolution of 2-5 $\mu$ m, taking up to 2 hours for each sample to acquire high-resolution mineral maps. Simpson et al., (2019) created mineral maps (*figure2.2*) by using a spectra-matching library between Energy Dispersive spectrometry (EDS) analyses and the EDS profiles of reference minerals. Various analyses, such as XRD and petrography, were used to constrain the classification as described by Simpson et al., (2019). Then mineral percentages were calculated from the mineral maps, see *appendix3* for the mineral percentage estimates.

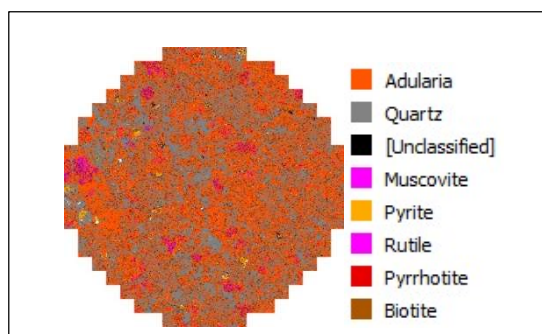


Figure 2.2: An example of a TIMA mineral map (in PNG format) for sample AU57565

## 2.2. Methods

Various methods were employed to understand spectral characteristics of feldspars and other associated minerals from the available rock samples. These methods include TIMA (PNG) image processing, LWIR image acquisition, pre-processing and processing, and data analysis and interpretation. These methods are explained in detail in the subsections below and summarized in a methodological flowchart in *figure2.3*.

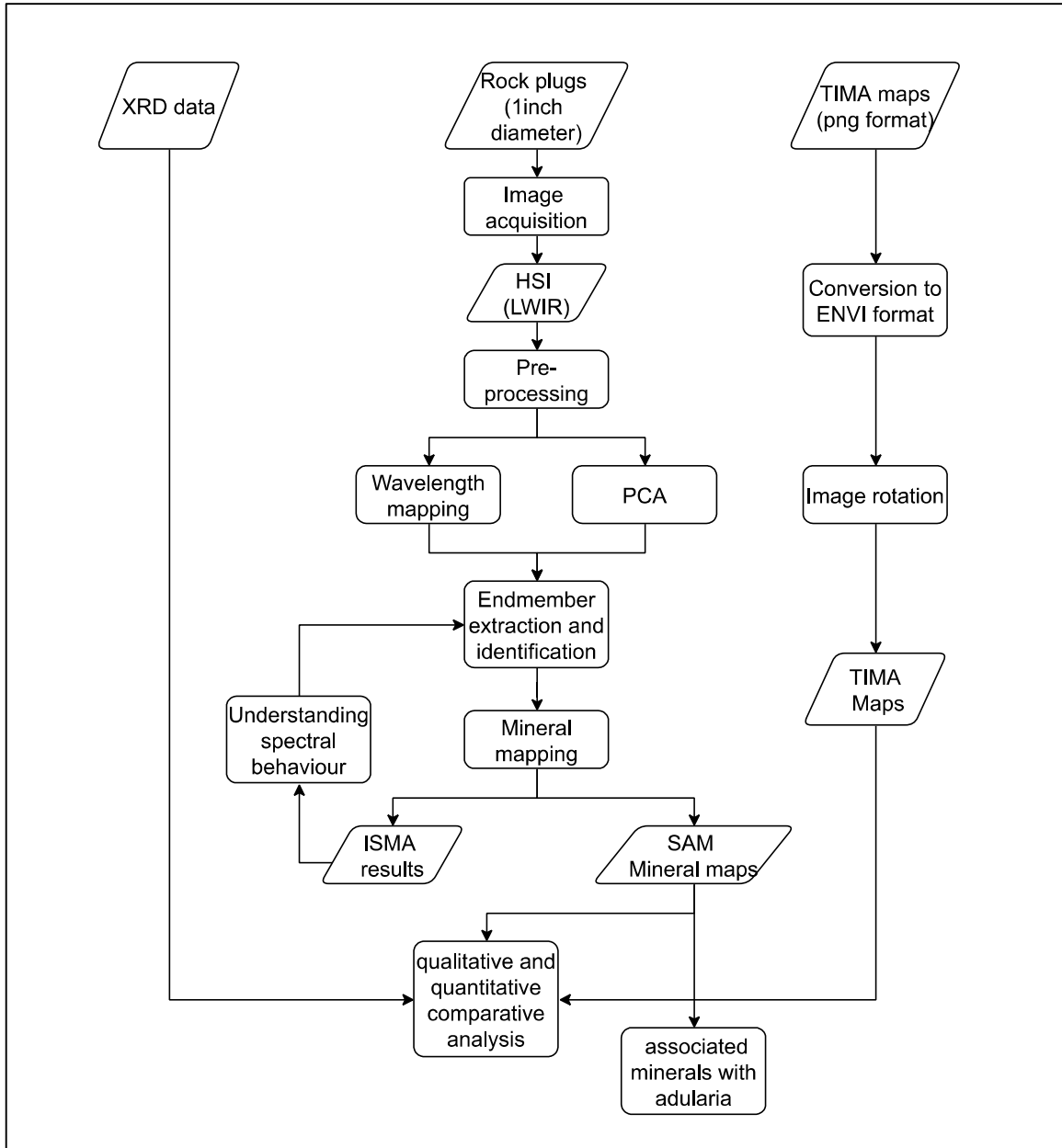


Figure 2.3: Methodological flowchart

### 2.2.1. TIMA (PNG) image processing

TIMA results were available as images in PNG format. These images were processed and converted to a suitable format for qualitative comparison with LWIR images. First, endmembers were extracted from TIMA images. Then, the extracted endmembers were used to classify TIMA images using Spectral Angle Mapper (SAM) algorithm (see section 2.2.6), creating mineral maps in Envi format. These maps had clear mineral patterns and texture that were used as markers to rotate them in the direction that was easily compared with LWIR images.

### 2.2.2. Hyperspectral image (HSI) acquisition

High-resolution hyperspectral images were acquired on 50 polished rock samples aiming at detecting variation in spectral features with their corresponding wavelength positions. Data acquisition took place at BGR (Bundesanstalt für Geowissenschaften und Rohstoffe) in Hannover, Germany, using a sisuROCK hyperspectral imaging system. The imaging system was set in LWIR spectral range, with a spatial resolution of 400 $\mu$ m. Table 2.1 presents specification of the LWIR camera used.

OWL 3	LWIR wavelength range
Location	BGR
Wavelength range (nm)	7704.44 to 12571.9
Pixel size ( $\mu$ m)	400
Number of bands	101
Frame rate	12.55
Exposure time	0.97

Table 2.1: Specification for an OWL 3 imaging system

The polished rock samples were placed horizontally, attaining the same level/height on a black wooden plank, as shown in *figure2.4*. These samples were scanned in groups; therefore, a total of eight hyperspectral images named Kar01- Kar08 were acquired.



Figure 2.4: Rock samples on a wooden plank (a yellow arrow showing the scanning direction -top of the HSI)

### 2.2.3. Hyperspectral Image pre-processing

The acquired hyperspectral data included striping, dropouts and miscalibration, resulting in noisy bands. The first pre-processing steps were done by Dr. Martin Schodlok (BGR, Germany) using standard OWL processing chain version 4.10. These steps include raw data conversion and destriping. Conversion of raw data (DN values) into reflectance values was done using a diffuse reflecting aluminium standard and dark current measurements on a blackbody. Destriping was done to improve the signal to noise ratio of the hyperspectral image before further image processing and analysis, i.e., endmember extraction. This took into account the preservation of spatial and spectral features while minimizing the noise.

For additional noise reduction, I performed spectral subsetting and Minimum Noise Fraction (MNF) transformation. First, a spectral subset was performed to remove the noisiest bands at the periphery of the spectral range. Number of bands reduced to 97 bands corresponding to the wavelength range 7806nm to 12475nm from the original 101 bands after the removal of the first and the last three bands. Afterward, MNF, a linear transformation, was employed on the spectrally subsetting image files to segregate and suppress noise while preserving spectral features (Green, Berman, Switzer, & Craig, 1988). Forward MNF transform was employed first, resulting in output MNF bands and eigenvalue plots. Individual output bands and their corresponding eigenvalues were visually inspected to select components with the most information. Low order components appeared to contain most of the information and less noise. Therefore, an eigenvalue of 3-3.5 was used as a cut-off point for all images to select output MNF bands/components. The cut-off point varied from 3 to 3.5, given different images that may have been subjected to a different level of noise. The selected components for each image (typically about 7 to 11 components) were used to perform inverse MNF to transform MNF bands back to their original data space of 97 bands. Masking was done on the reflectance image during MNF transformation to remove unwanted space outside the sample margin that could affect the noise statistics. The masks were built using region of interest (ROI) defining the sample image. Finally, the image data cubes with less noise compared to the original data cubes were produced.

Further processing steps, such as wavelength mapping, as suggested by Abera, Hecker, & Bakker, (2018), requires conversion of reflectance to emissivity values for LWIR image files. This is done to avoid highlighting features that are not representative of minerals present in the investigated dataset. Wavelength mapper performs normalization using the highest reflectance/emissivity values prior to identifying band position and depth of local minima. For the case of LWIR reflectance and emissivity data, wavelength mapper tends to highlight reflectance lows and emissivity minima, respectively. However, emissivity minima are typical diagnostic features. Therefore, the corrected reflectance data were converted to apparent emissivity values based on Kirchhoff's law ( $\epsilon = 1 - r$ ) using the band math tool. Equation (i) was used for the conversion.

$$\left( \frac{1000.0 - b1}{1000.0} \right) \dots\dots\dots (i)$$

b1- assigned to a single variable, an image file

**Endmembers**

Endmember extraction is a crucial step to image classification. It involves the extraction of distinct spectral signatures from a sample image, representative of minerals. Manual endmember selection approach was used to create a direct association between endmembers and image in further processing steps, i.e., mineral mapping, as suggested by Borengaser, William, Watkins R., & Michael T. Eismann, (2012). Various algorithms were performed on the pre-processed LWIR image to enhance distinct spectral features and facilitate the manual endmember selection. Below is the description of the two algorithms used, Principal component analysis (PCA) and wavelength mapping.

**2.2.4. Principal component analysis (PCA)**

PC analysis is a technique used to enhance and compress the image; therefore, it provides a small number of components based on its variance. This technique is done through the rotation of a new set of orthogonal axes, as a result, maximizes the data variance (Green et al., 1988). To manually select endmembers, forward PC rotations were performed on the pre-processed LWIR image to produce uncorrelated output bands. The first PC bands contain the most significant percentage of data variance, thus appears to contain most information compared to the last PC bands. Therefore, the first six principal components/output bands were selected. Different RGB band combinations were used to display the most contrast images from which coordinates (x,y) corresponding to various endmembers were manually picked. These coordinates were later on used on the pre-processed LWIR image to extract endmembers.

**2.2.5. Wavelength mapping**

Wavelength mapping method was employed as a second source to facilitate the manual endmember selection from the pre-processed LWIR image files. This method is a two-step approach that highlights wavelength position of the deepest features (emissivity minima) representative of dominant minerals per pixel. The resulting maps are fused images of interpolated wavelength position of the local minima and their corresponding depth displayed in a Hue Saturation Value (HSV) colour ramp.

Wavelength mapping method was performed on 8 LWIR sample images. The selection of these samples was based on the presence of feldspar minerals, which was the main focus of this study using TIMA maps and their corresponding mineral abundances. Step 1 was run to obtain the wavelength position of the deepest emissivity minima in the wavelength range of 7800nm to 11500nm. Continuum removal by division was applied during this step to normalize the spectrum (Hecker, van Ruitenbeek, van der Werff, et al., 2019).

Step 2 was run on the minimum wavelength image obtained from step 1 with a wavelength stretch and a depth stretch. Wavelength stretch was of 8000nm to 10500nm, targeting diagnostic features for feldspars and other associated minerals, while depth stretch was set from 0.0 to 0.05, given the lower depth of spectral features (less than 10%). Finally, spectral signatures highlighted by various colours corresponding to a specific wavelength position of the local minima were selected and added in the endmember list.

### **2.2.6. Endmember extraction and Identification**

Manually picked endmembers from the pre-processed LWIR data cubes were selected. PCA results and wavelength maps aided the endmember collection process (see, section 2.2.4 and 2.2.5 above) as it enhances spectral information with varying spectral features at different wavelength positions (Hecker, van Ruitenbeek, van der Werff, et al., 2019; Hecker, van Ruitenbeek, Bakker, et al., 2019). Fifty initial spectral endmember candidates were extracted based on the PCA and wavelength mapping products. Afterward, they were sorted based on their similarities and visually inspected to remove duplicates. Finally, 12 unique endmembers out of the initial 50 endmember candidates were selected based on the PCA and Wavelength Mapping products.

Determination of mineralogical composition and naming of the 12 endmembers using the knowledge of diagnostic spectral absorption features followed. The approach used was spectra matching between the endmembers and existing spectral libraries in continuum removal. The spectral libraries used were open access USGS, JHU, ASU and CSIRO library and a chalcedony reference spectra provided by Dr. Steven Ruff. A list of expected minerals from TIMA results presented by Simpson et al., (2019), and lookup tables for wavelength position of minerals presented by Fagbohun, (2015) was used to narrow down the search of minerals from spectral libraries to match with the endmembers. Thus mineral identification and naming became less challenging. Finally, 12 identified endmembers with their respective spectral features were described and summarized in a table. A spectral library that was used in mineral mapping was also created from this endmember collection.

### **Mineral mapping**

Mineral mapping involves assigning a particular mineral class to a specific pixel resulting in a mineral map. This determines spatial distribution of minerals as well as quantification of minerals. Mineral mapping was done through image classification approach. Two different algorithms were employed, spectral angle mapper (SAM) and Iterative Spectral Mixture Analysis (SMA) for mapping of dominant mineral per pixel and determining fractional abundances of minerals per pixel, respectively. Subsections below provide details on the two algorithms.

### **2.2.7. Spectral Angle Mapper (SAM)**

SAM classification algorithm is a technique that allows rapid mapping of the spectral similarity between image spectra and reference spectra. It determines the spectral similarity by calculating the angle (in radian) between the two spectra, treating them as vectors in feature space. For this dataset, the reference spectra used were the endmembers directly extracted from the pre-processed LWIR sample images. A single value of 0.05 radians was set during SAM classification to obtain a match. Also, SAM depends on an overall spectral fit rather than an individual emissivity minimum. A specific spectral range was therefore used to target specific features, as seen in the identified endmembers. Therefore SAM algorithm was performed on bands 1-57 and bands 68-82 corresponding to the wavelength ranges 7753-10478nm and 11014-11695nm. SAM output includes a set of rule images (one per endmember) that were used in the post-classification to adjust threshold angle values for each endmember to obtain realistic results. Rule image is an image that shows intermediate classification results for a selected mineral class.

Post classification was done on a set of rule images to have control over the classification results to reduce misclassification. The rule classifier tool was used to assign different thresholds for different endmembers based on histogram values, and random inspection of the pixels. This was to investigate the frequency plot of the classified pixel and filter out misrepresented pixels. Finally, mineral maps with 12 mineral classes per sample image were created from the ruled images. Mineral percentages were estimated from statistics calculated for every sample mineral map. SAM classification results were later compared in terms of spatial patterns and mineral percentages to TIMA and XRD results.

#### **2.2.7.1. Iterative Spectral Mixture analysis (ISMA)**

Spectral mixture analysis is a tool that analyses and determines the relative mineral abundance of mineral constituents per pixel using the purest endmembers. There are several spectral mixture analysis techniques; However, Iterative Spectral Mixture Analysis (ISMA) stands out. This technique has previously been used to addresses endmember's variability, performs subpixel classification, and calculates fractional abundances of mineral constituent. It uses the same principle as unconstrained linear unmixing, except the process is repetitive (Rogge, Rivard, Jinkai, & Jilu, 2006). Therefore, it removes irrelevant endmembers per iteration until a critical point is reached where only relevant endmembers remain.

ISMA was done in this study due to the presence of a large number of mixed pixels that were not correctly classified in the SAM mineral maps. First, sample pre-processed LWIR images were converted from band sequential (bsq) to band interleaved by line (bil) format since the process is done simultaneously on a block of data. Then IDL was used to perform ISMA on sample images using parameters displayed in *table2.2*. The number of lines in each block varied, given varying number of lines per image.

Parameters	Values
Number of lines in each block	varying
Maximum no of EMs	5
rms threshold	0.1
Iteration threshold	2

Table 2.2: Parameters for ISMA tool

A shade endmember, which is used as a multiplicative factor, is automatically added to the process and set to value 1. The process was fast given a less computational load due to the use of 12 endmembers, which was less than the number of spectral bands (97 bands). Finally, ISMA results, which include root mean square error (RMSE), removed and abundance images, were produced. RMS image calculated RMS error over each iteration. Removed image shows a specific endmember that was removed at each iteration for all pixels. Abundance image presents endmember's fractional abundances, shadow endmember (shade) fraction and RMS error. The fractional mineral abundances per pixel and sample image were determined from statistics calculated from the abundance images excluding the shade fraction and RMS error.

### 2.2.8. LWIR-TIMA-XRD comparative analysis

The LWIR mineral map, TIMA and XRD results were compared to assess LWIR spectroscopy in mapping of feldspars and other minerals present in this dataset. The approach used involved qualitative and quantitative comparative analysis. First, a visual comparison was done based on the spatial distribution of mineral in the LWIR and TIMA mineral maps. Samples with clear mineral patterns that were used as markers in the alignment of TIMA mineral maps in the direction of the LWIR mineral maps were used for this analysis.

Then, a quantitative comparison of the aggregated mineralogy of the samples was performed. It involved the use of mineral percentage estimates from SAM, TIMA and XRD data for adularia, albite, quartz and calcite. This analysis was done for 35 samples that were common in all datasets. Prior to performing quantitative comparison analysis, a summation of mineral percentage estimate was done to deal with duplicate classes. For example, for adularia mineral class, the mineral percentage was estimated by summing up the abundances of the two identified classes that were spectrally distinct enough to be mapped as separate classes. However, this did not apply to all classes, especially the mixed mineral classes. Therefore, SAM classified images were used in this analysis without accounting for the mixed mineral classes. However, an assumption was made to investigate the influence of mineral mixtures in mineral quantification. The assumption was that constituent minerals were of equal proportion; thus, for example, 50% of quartz\_illite mineral abundance was added to a quartz percentage estimate and the difference in relative mineral abundances was analyzed.

The approach used for quantitative comparative analysis was correlation analysis, a statistical method that evaluates strength of the relationship between two quantitative variables. A high correlation means the variables highly relate to each other, and vice versa is true. This was done by plotting mineral abundances of LWIR results against TIMA and XRD data. Then the coefficient correlation was calculated and analyzed for each plot. This was based on the general trendline (regression line) drawn based on sample distribution depending on their respective mineral abundances in both datasets. Therefore, the performance of LWIR spectroscopy, together with the methodological approach used, for example, in mineral mapping, e.g SAM, was assessed.

#### **2.2.9. Establishing mineral assemblage for adularia-rich areas.**

Mineral assemblage for adularia-rich areas includes other hydrothermal minerals that are commonly associated with adularia and can, therefore, be used to identify adularia-rich areas. The approach used to determine hydrothermal minerals that commonly occur with adularia was based on their spatial association with the occurrence of adularia. Prior to that, sampling was done to select samples that are considered to be adularia rich. Adularia rich samples are defined by sample mineral maps with >30%adularia relative to other minerals. The definition of adularia-rich samples considered other methods such as XRF that can easily identify the presence of adularia only when samples have >30%adularia (Simpson et al., 2019). Therefore, samples were sorted and filtered from largest to smallest based on the adularia % estimates. 10 of 50 samples were selected as adularia rich samples. An observation was made on classified pixels close to adularia classified pixels to determine minerals that are spatially associated with adularia. Finally, dominant minerals that are associated with adularia in the selected samples were highlighted. Also, adularia was plotted with albite mineral abundances to assess their occurrence and comment on whether their relationship can be used in permeability studies. Given that adularia and albite are associated with high permeability and low permeability zones in geothermal systems, respectively.

### 3. RESULTS

#### 3.1. Image pre-processing results

Output MNF bands of the hyperspectral image and eigenvalue plot obtained after forward MNF transformation are displayed in the figures below. The number of selected components varied from one image to the other from 7 to 11 components. The selection was based on inspection of MNF output bands and eigenvalues. *Figure 3.1a* is an example of a sample image from 50 acquired LWIR images, sample AU57602, which illustrates the level of information/noise per component. The result shows an increase in noise with increasing number of components. *Figure 3.1b* shows an eigenvalue plot where eigenvalue three was selected as a cutoff point. At this point, there is a dramatic increase of eigenvalues, which reflect the increase in data variance. Transformed bands beyond the cutoff show no change in their corresponding low eigenvalues. Therefore, only the first seven components were selected for the inverse MNF transformation.

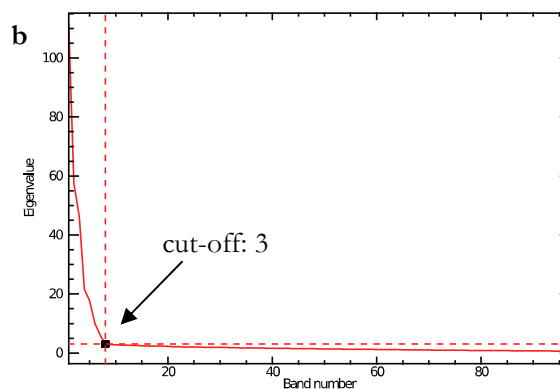
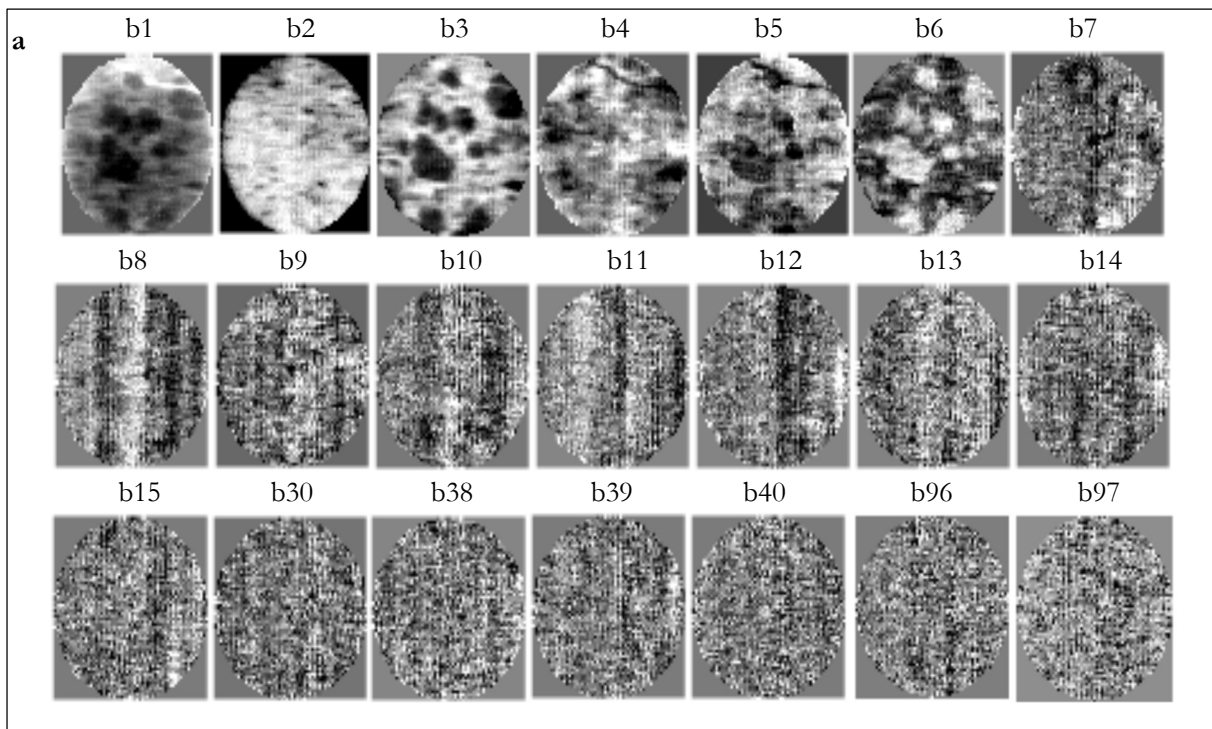


Figure 3.1: a) MNF output bands and b) eigenvalue plot for sample AU57602

Noises were suppressed after the application of forward and backward MNF. The noise suppression is demonstrated in reflectance spectra, as shown in *figure3.2a*. Spikes that appear as minor features in the original reflectance spectrum (solid line) were removed in the resulting spectrum (dotted line) of the same pixel location. The resulting spectrum (dotted line) appears smooth with visible spectral features within a spectral range of 7806nm and 12475nm. The spectral range was reduced to 7704.43 to 12571.9 nm due to noisy bands through spectral subsetting. Also, an exponential increase of reflectance values from  $\sim 10500$ nm was observed and appeared consistently in all sample images, as observed in *figure 3.2a*. *Figure3.2b* demonstrates an emissivity spectrum obtained after the reflectance to emissivity conversion.

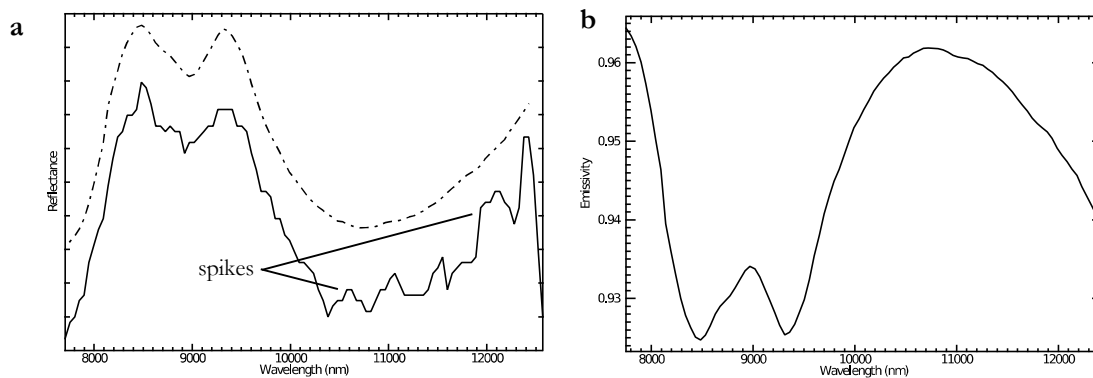


Figure 3.2: a) Reflectance spectra(offset for clarity) before (solid line) and after (dotted line) forward and backward MNF transformation b) emissivity spectrum after reflectance to emissivity conversion

### 3.2. Principal Component Analysis (PCA) results

Forward PC analysis resulted in uncorrelated image bands, also known as PC bands. The first six bands contain most of the information; therefore, they were used in a band combination image to highlight spatial and spectral distinct features per sample image. *Figure3.3* displays an example of sample images AU57491 and AU57602 with band combination 135 and 321, respectively. The images had spatial and spectral contrast displayed in different colours that were used to extract endmembers. However, only very distinct colours displayed distinct spectra. For example, the deep green and pale/yellowish-green in sample AU57491(left) had the same spectra signature.

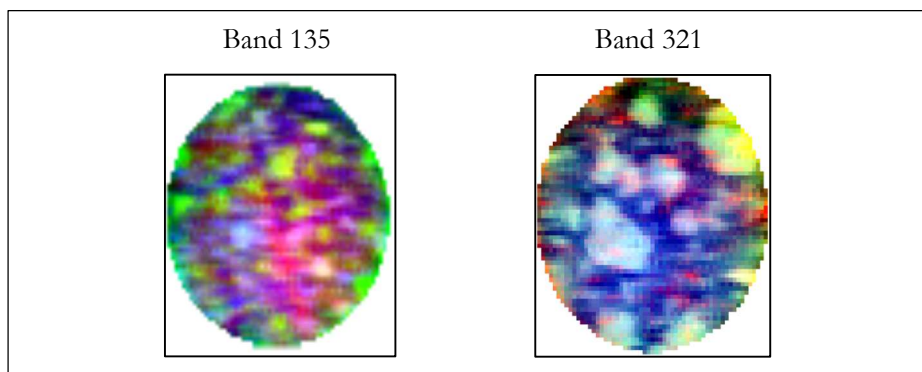


Figure 3.3: Band combination RGB= PC135 and PC321 for sample AU57491(left) and AU57602(right)

### 3.3. Wavelength Map

Wavelength maps of 8 sample images were produced for a wavelength interval of 8000nm to 10500nm with a depth stretch of 0 to 5% emissivity. Results show a spatial and spectral contrast corresponding to different colours representative of different wavelength position. For illustration, *figure3.4* demonstrate wavelength maps of AU57491 and AU57602 sample images. Maps are highlighted by blue, cyan and yellowish colours corresponding to wavelengths ~8100nm, 8400nm, and 9400-9600nm, respectively. For sample image AU57602, quartz and adularia2 extracted from the wavelength maps were highlighted by yellowish and blue colour.

Less spatial contrast was observed relative to spectral contrast. *Figure3.5* presents spectra extracted from a wavelength map of sample AU57491 (*figure3.4*), which show different spectral signatures highlighted by the same colour. It is because spectral signature of different minerals present in this particular sample image had their deepest features at the same wavelength position. Quartz spectrum and a mixed (unidentified) spectrum highlighted by blue colour had their deepest feature at ~8100nm, see *figure3.5*. As highlighted in the map, their features are at the same wavelength position despite differences in their shape, which is not highlighted in the wavelength map. Also, a spectrum highlighted by cyan colour in the wavelength map with its deepest feature at ~8400nm suggests that it is a mineral mixture (*figure3.5*). The spectrum exhibit subtle emissivity peaks at ~8600nm and ~9000nm, shown by arrows in *figure3.5*.

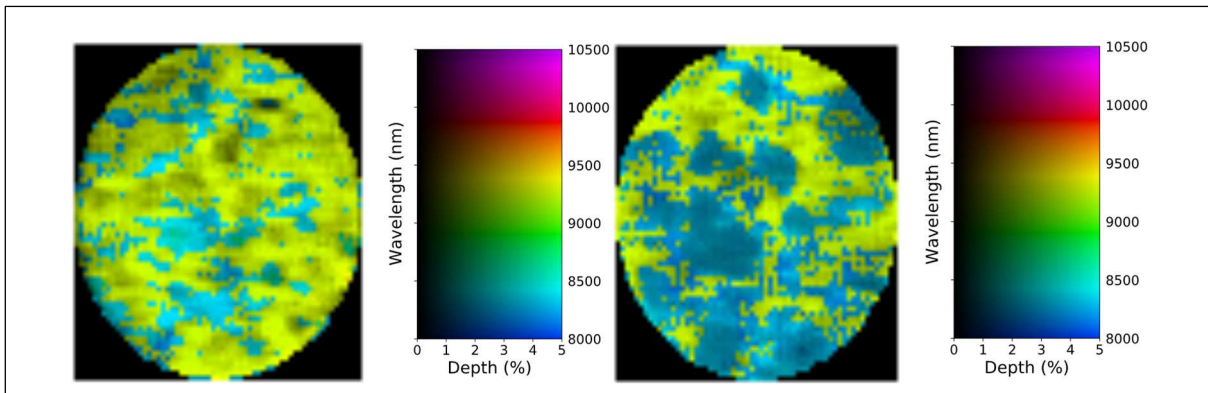


Figure 3.4: A wavelength map for AU57491 (left) and AU57602 (right)

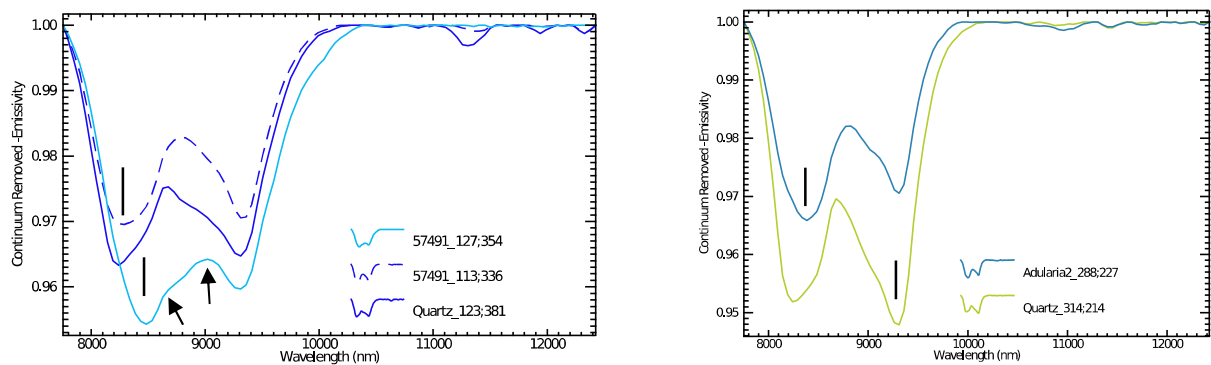


Figure 3.5: Spectra from wavelength maps of AU57491(left) and AU57602 (right) corresponding to colours highlighted in the maps in figure3.4 (Vertical lines show emissivity minima and arrows shows emissivity peaks)

### 3.4. Endmembers

Twelve unique endmembers were identified. The endmember's spectral signature differs in shape and wavelength position of their emissivity minima and emissivity peaks. Their diagnostic spectral features are within the reststrahlen band (8000nm to 11500nm), as summarized in the *table3.1*. The identified endmembers include quartz, adularia, orthoclase, albite, anorthoclase, calcite, diopside, oligoclase and mixed spectra. Among the mixed spectra, quartz+ illite and quartz+ calcite were identified. However, some of the extracted mixed spectra with overlapping features were insufficiently distinct nor included in the endmember list. The endmembers, together with existing reference spectra from various spectral libraries, i.e., USGS, JHU, ASU and CSIRO, are described in detail in the subsections below. They are categorized into two groups, feldspars and other associated minerals present in this dataset. In general, emissivity spectra in continuum removal shows a minor shift in the wavelength position of the spectral features to shorter wavelengths.

#	Endmembers	Spectral characteristics
1	Albite	displays four spectral features. The first occurs at 8726nm and the second subtle spectral feature is at 9213nm, followed by a weak doublet at 9554nm and 9797nm. The 9554nm is the deepest feature.
2	Oligoclase	displays spectral features at 8629nm(the deepest) and 9602nm with emissivity peak at 9310nm. It also exhibits a calcite related feature at 11306nm.
3	Calcite	displays a diagnostic feature at 11355nm and two subtle features at 9262 and 9748nm.
4	Anorthoclase	displays two asymmetrical spectral features with emissivity peak at 8921nm. The first occurs at 8434nm, and the second deep feature is centered at 9602nm.
5	Orthoclase	display two spectral features at 8434 (rounded) and 9456nm (sharp) with emissivity peak at 9018nm.
6	Adularia1	display two spectral features at 8434nm and 9554nm. The emissivity peak is at 9018nm.
7	Adularia2	has spectral features at 8434nm and 9310nm and emissivity peak at 8823nm.
8	Diopside	first deep wide diagnostic feature within ~9000nm and 9250nm and multiple features at 10235nm, 10770nm, 11501nm and 11890nm.
9	Quartz	displays two spectral features at 8239nm and 9310nm with emissivity peak at 8629nm.
10	Quartz_Illite	It is characterized by three spectral features at 8434nm, 8823nm and 9310nm. The emissivity peak is at 8629nm.

11	Calcite_quartz	displays features that were present in calcite and quartz endmember. Features were at 8288nm, 9268nm and 9748nm (subtle) and a calcite related feature at 11306nm. The emissivity peak is at 8629nm.
12	Chalcedony	displays two asymmetric features at 8385nm(round) and 9262nm (the deepest) with emissivity peak at 8629nm.

Table 3.1: Description of the 12 selected endmembers

### 3.4.1. Feldspar minerals

Generally, the identified feldspar minerals exhibit spectral features in the wavelength range of 8100nm to 10400nm and appear to have broad spectral features, particularly plagioclases when compared to alkali feldspars. Two plagioclase were identified as albite and oligoclase.

**Albite** exhibit an emissivity peak at 9018nm, emissivity minimum at 8726nm and multiple features at 9213nm, 9554nm and 9797nm (*figure 3.6a*). The multiple features distinctively distinguish albite from oligoclase. However, the multiple features observed in albite were not pronounced as much as in its corresponding reference spectrum (CSIRO). The reference spectrum for albite had a feature at 8726nm and multiple features at 9164nm, 9602nm and 9894nm.

**Oligoclase** is characterized by diagnostic spectral features at 8629nm and 9602nm, with its emissivity peak at 9310nm (*figure 3.6b*). The reference spectrum for oligoclase (CSIRO) appears more symmetrical compared to the oligoclase image spectrum with diagnostic features at 8726nm and 9894nm. It may be attributed to the mixture as the oligoclase image spectrum exhibits another feature, carbonate-related at 11306nm. In comparison to the reference spectra, albite and oligoclase present in this dataset had minor shifts of their second features while maintaining the same wavelength position for their first feature and emissivity peak.

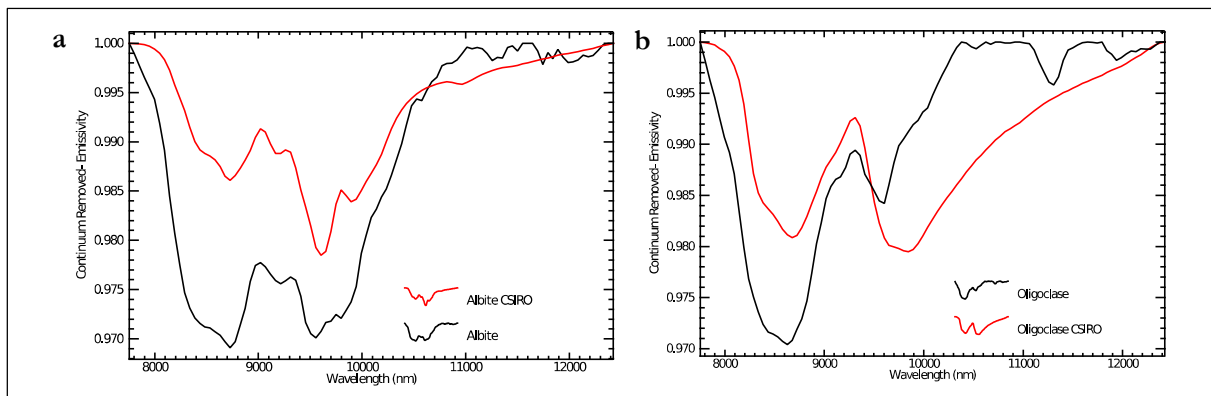


Figure 3.6: Plagioclase spectra from LWIR images (black) versus reference spectra (red) from an existing spectral library

Alkali feldspar minerals identified include adularia, orthoclase and anorthoclase. In this dataset, two different adularia were observed named **adularia1** and **adularia2**, see (figure3.7a). Both adularia spectra did not have a perfect match with the existing reference spectrum presented in figure3.7b. The **adularia** image spectrum had minor shifts to shorter wavelengths in their emissivity peak and minima. Figure 3.7b shows the adularia reference spectrum from CSIRO (dotted) with three features at ~8800nm, 9200nm and 9400nm while the spectrum from usgs (solid) shows two doublet features at 8434, 8677nm and 9507, 9846nm with emissivity peak at 9067nm. In contrast to the reference spectra, adularia1 has an emissivity peak at 9018nm and emissivity minima at 8434nm and 9554nm. Adularia2 is characterized by an emissivity peak at 8823nm and emissivity minima at 8385nm and 9310nm, as shown in figure3.8a. In comparison to adularia1, adularia2 had spectral features at shorter wavelengths. However, both adularia1 and adularia2 were consistent in terms of their feature's position in various adularia rich rock samples.

**Orthoclase** had an emissivity peak at 9018nm and emissivity minima at 8434 and 9456nm (figure3.7c). In comparison to the reference spectrum (JHU), orthoclase had no split feature for the first emissivity minima as it appeared in the reference spectrum. Otherwise, they both had a similar shape and wavelength positions of their spectral features. Figure3.7d presents **anorthoclase**, which appears to have asymmetrical spectral emissivity minima at 8434nm and 9602nm with its emissivity peak at 8921. In comparison to anorthoclase reference spectra (CSIRO), the features were at similar wavelength positions except for the shape of the second feature, which appears deep with sharp V-shape.

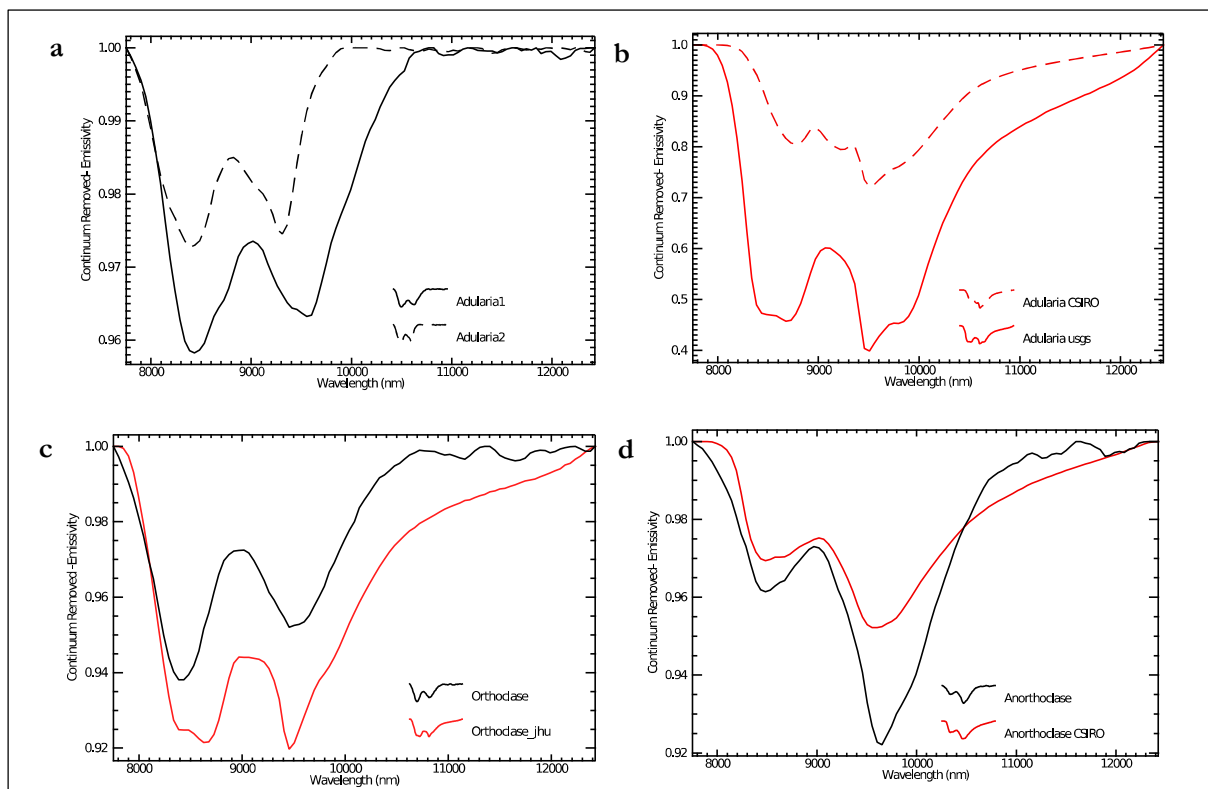


Figure 3.7: Alkali feldspar spectra from LWIR images (black) versus reference spectra from spectral libraries (red)

In general, the identified adularia spectral features appear to be distinct from other feldspar minerals in terms of their wavelength position, e.g., of emissivity minima for albite, emissivity peak for oligoclase, emissivity minima and peaks for anorthoclase. Also, adularia differs from anorthoclase in terms of their shape as well. An orthoclase spectrum appears to have a close resemblance to the adularia1 spectrum.

### 3.4.2. Other associated minerals

Other minerals identified in this dataset are silica minerals, calcite, diopside and a mixture of quartz+illite and quartz+calcite. Silica minerals include quartz and chalcedony. **Quartz** appears to be common in this dataset. The quartz spectrum has a diagnostic emissivity peak at 8629nm and minima at 8239nm and 9310nm (*figure3.8a*). In comparison to the reference quartz spectrum (USGS) (*figure3.8b*), there was a minor shift on the second emissivity minima from ~9200nm to 9310nm. **Chalcedony** displays asymmetric features at ~8385nm (round) and 9262nm (the deepest) with emissivity peak at 8629nm. It has a good match with chalcedony reference spectrum provided by Dr. Steven Ruff (ASU), as demonstrated in *figure3.8d*. The similarity between chalcedony and quartz is in terms of their wavelength positions. However, the main difference appears to be the shape, where chalcedony has more rounded features compared to quartz.

Moreover, quartz emissivity peak appears to persist in most mixed spectra, with a shift of its first emissivity minima towards longer wavelengths, from ~8200nm to 8434nm. It is observed in a mixture of **quartz with illite** (*figure3.8e*) and **quartz with calcite** (*figure3.8f*). **Illite** reference spectrum in *figure3.8e* exhibits diagnostic features at 8823nm and 9310nm, which is observed in the mixed spectrum of quartz and illite. **Calcite** had a diagnostic feature at 11355nm with two minor features at 9262 and 9748nm. In comparison to calcite reference spectrum (CSIRO), these minor features were more pronounced in the calcite image spectrum see (*figure 3.8g*).

Another mineral is **diopside**, a monoclinic pyroxene mineral with composition  $MgCaSi_2O_6$ . It has a deep and wide diagnostic feature within ~9000nm and 9250nm, which had a match with its corresponding reference spectrum (CSIRO) (*figure3.8h*). Features at longer wavelengths, as summarised in *table3.1* had no match with its corresponding reference spectrum.

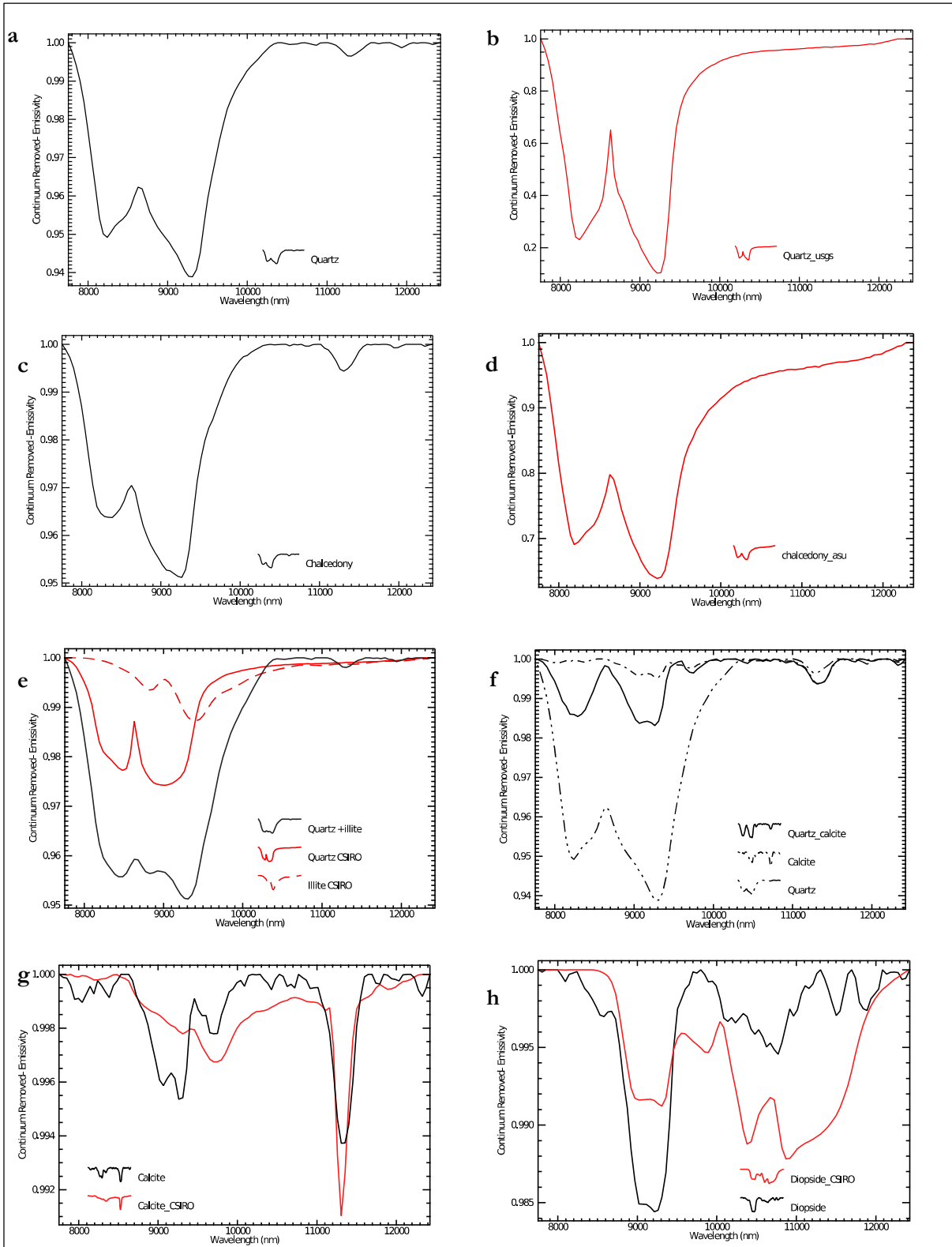


Figure 3.8: Spectra from LWIR images (black) compared with reference spectra from the existing spectral library (red)

### 3.5. Mineral mapping results

#### 3.5.1. SAM classification results

Mineral maps for LWIR images of the 42 rock samples were produced. Minerals were mapped for the 12 spectral endmembers, which include plagioclases, K-feldspars, quartz, calcite, and a mixture of quartz, calcite and clay minerals. Mineral abundances per sample image were estimated, see *appendix2. Table3.2* shows an example of mineral percentage estimates for few samples. Duplicate classes, for example, adularia1 and adularia2 percentage estimates, were summed up to estimate adularia mineral percentage. This was because adularia1 and adularia2 were distinct enough to be mapped as separate classes in different image samples, for example, in AU57504 and AU57555. For samples that had both classes, one endmember became dominant over the other, showing a significant difference in proportion. For example, in sample AU57598 and AU57602, adularia2 is >30% while adularia1 is <1.3%. Except for few samples that had both adularia1 and adularia2 in almost equal proportion, i.e., AU57565.

AU#	Mineral abundance (%)												
	Unclassified	Adu1	Qz-l	Cal	Or	Olg	Di	Adu2	Ab	Qz	Qz_cal	Ano	Chalc
57504	67.43	13.3	5.97		2.23	0.48			0.15	9.32	0.15		0.97
57555	1.85	60.29	0.26		0.46	1.43			18.02	0.33	1.24	15.97	0.16
57565	61.56	11.4		0.09		13.09	8.04	0.28	0.22	5.11		0.22	
57598	25.95	1.28				17.57	53.17	0.94	0.03	0.94		0.13	
57602	43.37	0.06					36.97		18.12	1.45		0.03	

Table 3.2: Mineral abundance for few sample images

The results show that not all pixels within a sample image are classified. However, the classified pixels cover at least 50% of a sample image for 26 images, e.g., AU57555 and less than 50% for the remaining 16 images, e.g., AU57504. Most of the unclassified pixels correspond to spectral signature that does not resemble the selected spectral endmember. *Figure3.10* shows an example of a spectrum extracted from the sample image AU57504 corresponding to unclassified pixels. It is insufficiently distinct as it resembles spectral endmember in terms of the wavelength position for mixed quartz due to a shift of the first feature from ~8200nm to ~8400nm. However, the peak appears wide and flat, suggesting a possible overlap of minerals due to spectral mixing; therefore, it became difficult to identify the mixed pixel.

Based on random pixel inspection, some pixels were classified as both adularia1 and orthoclase. Their close spatial association is also observed on minerals maps of, for example, AU57555 and AU57504. Similarly, some albite classified pixels were also classified as oligoclase and anorthoclase. For illustration purposes, *figure3.9* shows various LWIR maps for different sample images.

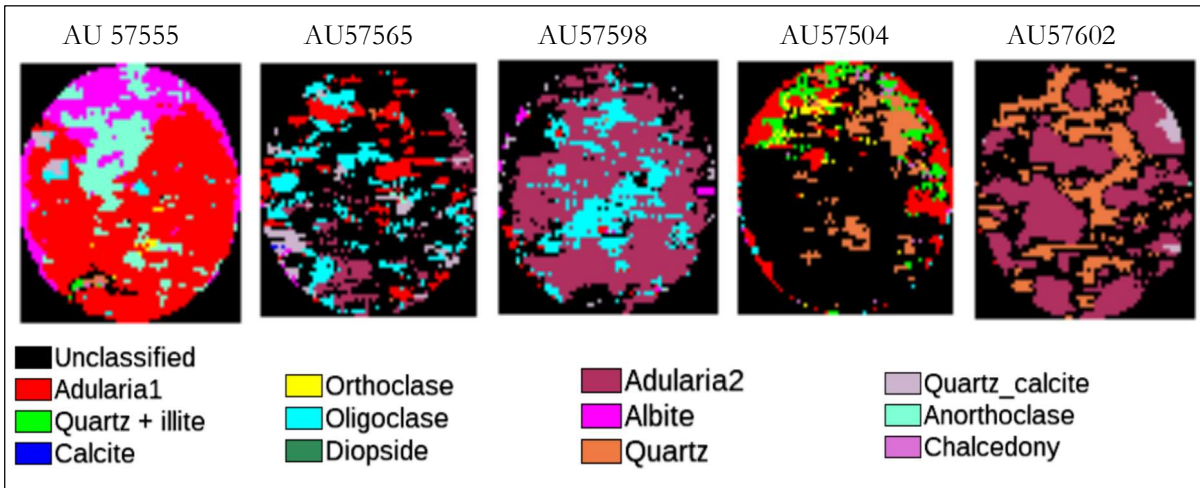


Figure 3.9: LWIR mineral maps for various rock samples

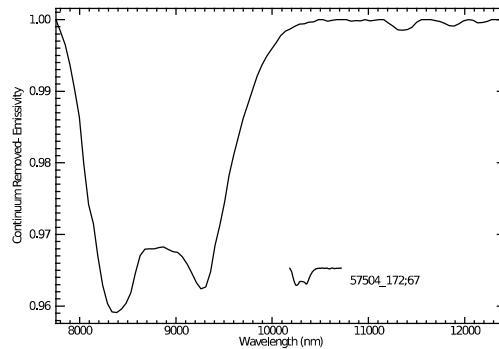


Figure 3.10: Spectra from AU57504 corresponding to unclassified pixel in the mineral map

Mineral textures were observed on few mineral maps, as shown in *figure 3.11*. These are veins that were also observed in rock samples. The veins cut across the rock samples at approximately 1mm width. The veins are mapped as calcite with quartz at its periphery in AU57540B; quartz and chalcedony at the periphery in AU57568. Based on random inspection of the pixels within the veins using the knowledge of the mineral diagnostic features, the spectra appear as a mixture of the two minerals, quartz\_calcite (refer to *figure 3.8f*).

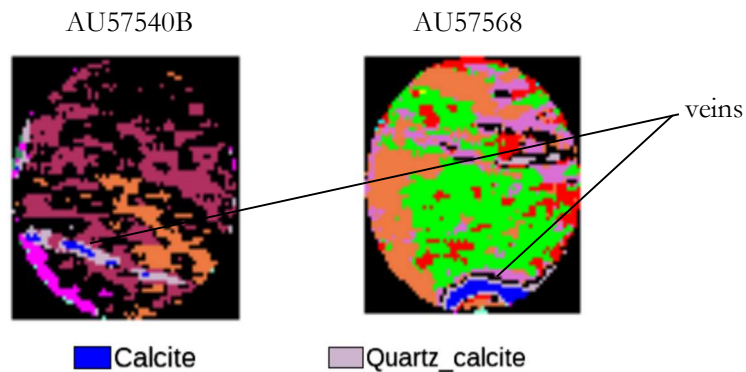


Figure 3.11: Veins (~1mm width) in LWIR maps.

Figure 3.12 demonstrates the influence of mineral mixtures in SAM mineral quantification. The chart shows mineral estimates for quartz before accounting for the mineral mixtures (the inner circle) versus mineral estimate for quartz after 50% of the mixed classes, i.e., quartz\_illite and quartz\_calcite, was added to the quartz percentage estimate (outer circle). The difference in quartz percentage varies from ~0-4%, as seen in the chart and goes up to 15% for other sample images.

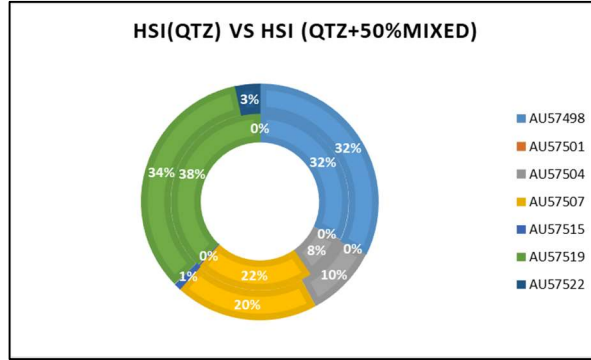


Figure 3.12: Percentage estimates of quartz(inner circle) versus percentage estimates of Quartz+50% mineral mixtures of quartz (outer circle)

### 3.5.2. ISMA results

ISMA analysis results present relative fractional mineral abundance per pixel. The result shows both negative and positive values for various endmembers. For example, sample AU57535 in table 3.3, basic statistics show negative and high positive values ranging from ~ -1.28 to 1.33. The root mean squared (rms) error is approximately zero. Shadow endmember(shade) has fractional abundances per pixel as well, but in most pixels, it appears to have negative values.

No.	Statistics	Fractional abundance			
		Min	Max	Mean	StdDev
1	Adularia1	-1.28	0.33	-0.00	0.05
2	Quartz+illite	-0.95	1.33	-0.01	0.10
3	Calcite	-0.88	0.19	-0.02	0.09
4	Orthoclase	-0.44	0.63	0.14	0.17
5	Oligoclase	-0.70	0.43	-0.12	0.19
6	Diopside	-0.41	0.31	-0.02	0.06
7	Adularia2	-0.46	0.59	0.01	0.10
8	Albite	-0.34	0.00	-0.00	0.01
9	Quartz	0.00	1.54	0.84	0.24
10	Quartz+calcite	-0.81	0.40	-0.06	0.14
11	Anorthoclase	-0.33	0.50	-0.06	0.11
12	Chalcedony	-0.85	0.90	-0.16	0.23
13	Shade	-0.02	0.77	0.47	0.12
14	rms	0.00	0.00	0.00	0.00

Table 3.3: Unmixing results for sample image AU57535

For the rest of the endmembers, the results show positive fractional abundances only for few image pixels. For these pixels, the fractional abundances summed up to less than one, as shown in figure 3.13a, excluding

the shadow endmember. However, other pixels had negative values, which made it difficult to determine its fractional abundance for the minerals present in the specific pixel. These pixels, with negative values, also appear to have high false-positive values, as shown in *figure 3.13b*. Pixels with positive fractional abundances for various minerals/endmembers were inspected to see whether they contribute to the spectral signature of that pixel. The results shows similarity between spectral diagnostic features of individual minerals and that of the mixed spectrum per pixel, as shown in *figure 3.13a(right)*. Band 9, 11 and 13 in the abundance profile represent endmember quartz, anorthoclase and shadow endmember, respectively.

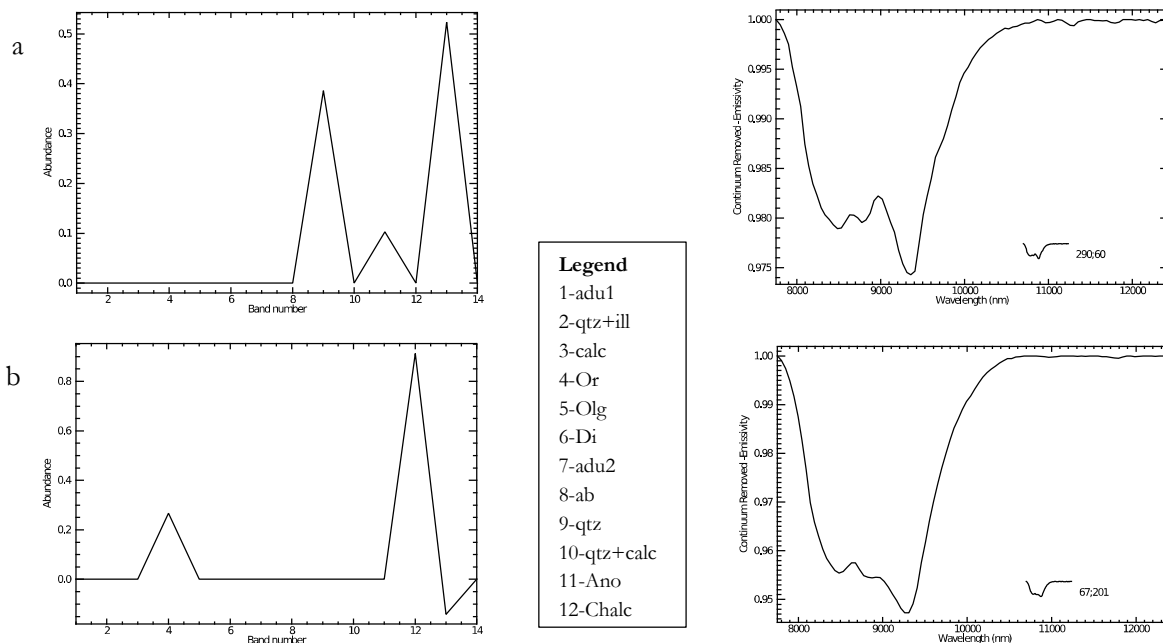


Figure 3.13: Abundance profile for fractional abundances per pixel (left) with their corresponding spectral signature (right). This is for the pixel where ISMA worked.

Abundance images and their corresponding rms profile showed that pixels with less number of endmembers per pixel had a sharp increase of the rms values at lower band number/iteration. Therefore, the critical point occurs at higher rms values for a large number of endmembers per pixel. Based on random pixel inspection, pixels with negative values and a large number of endmembers tend to have a step up rms profile, as shown in *figure 3.14*. Thus it becomes difficult to locate the critical point where optimum number of endmembers is determined.

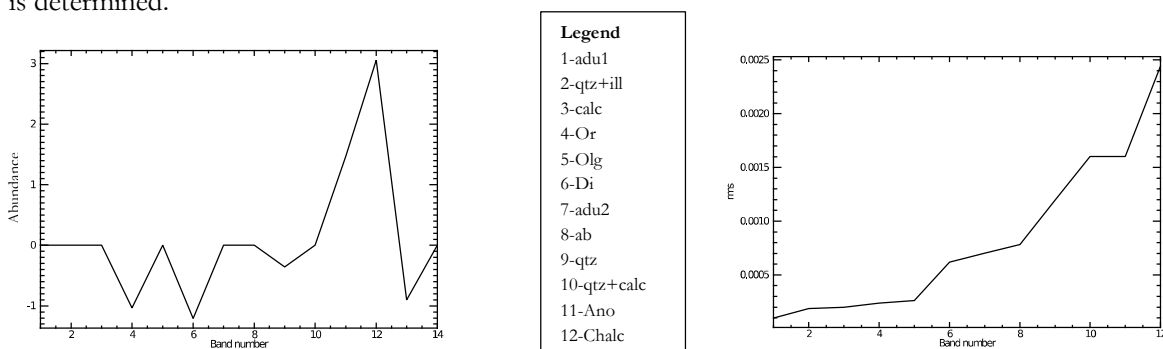


Figure 3.14: Abundance plots (left) of one of the problematic pixel with its corresponding rms profile (right)

### 3.6. Comparative analysis

The hyperspectral LWIR image results of this dataset are compared to auxiliary data sources in two ways: firstly, visual rock texture (spatial distribution of minerals) from the classification methods is compared with visual rock sample observations in TIMA mineral maps. Secondly, relative mineral abundances aggregated over the entire sample surface of the LWIR maps were quantitatively compared to those of TIMA maps and whole-rock XRD data. (see appendix 1, 2 and 3 for data).

#### 3.6.1. Visual comparison: HIS and TIMA

The comparison between LWIR (SAM mineral maps and wavelength maps) and TIMA maps focused on the spatial distribution of minerals. Six LWIR sample images had clear, comparable mineral patterns and therefore made it difficult to rotate and compare them with TIMA maps. However, for the few samples, there was enough similarity between LWIR and TIMA maps in patterns but not necessarily the mineral content per pixel. These include samples with structures such as veins. Common minerals are mapped in both LWIR (SAM) and TIMA maps, but there is a significant difference in their spatial distribution. Figure 3.15 shows sample which exhibits similar patterns in both datasets but differs in mineral distribution.

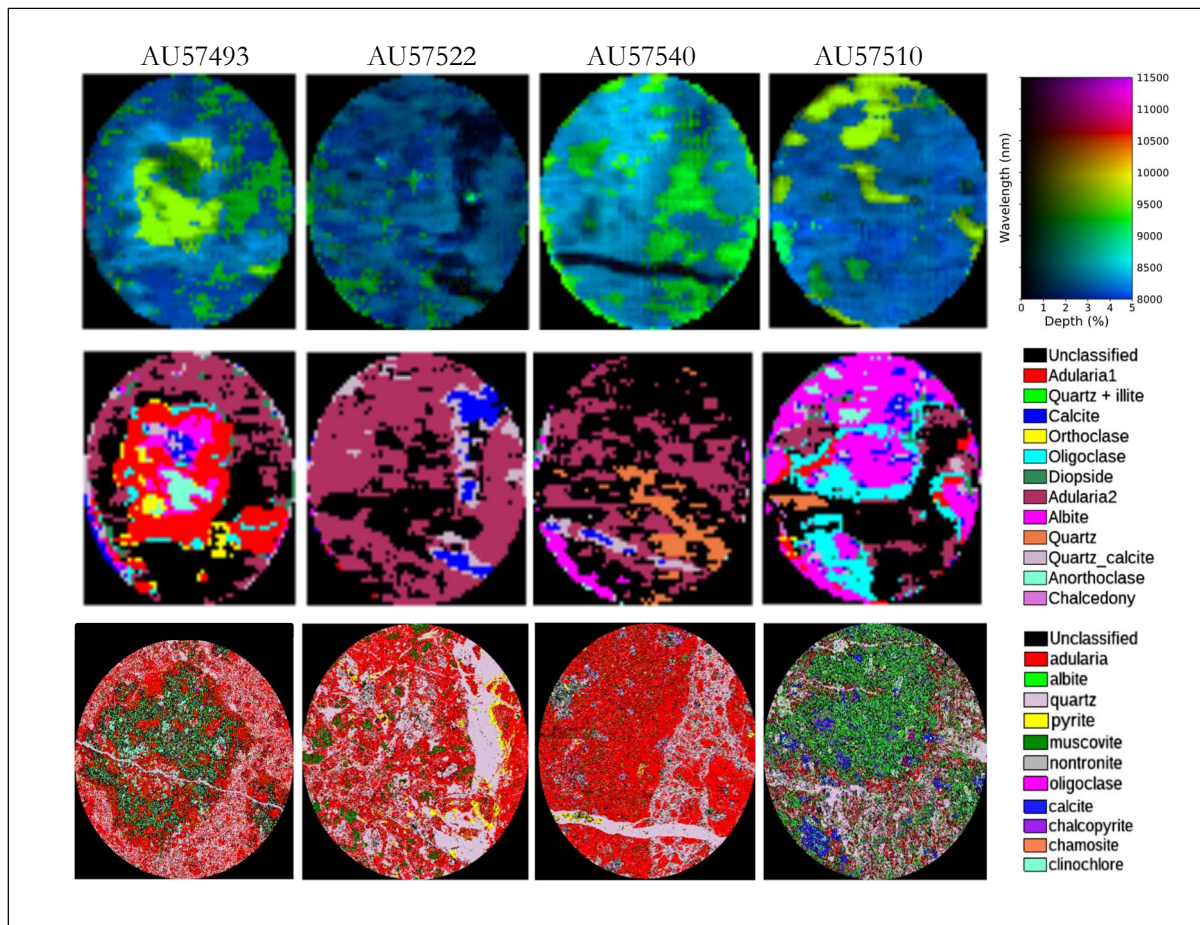


Figure 3.15: Comparison of the spatial distribution of minerals between wavelength maps, SAM classified images and TIMA maps for sample image AU57493, AU57522, AU57540 and AU57510

For example, AU57510, pixels classified as anorthoclase (light green) in LWIR (SAM) maps are classified as albite (green) in TIMA maps despite the similar pattern. Adularia ring (red) in the TIMA map for AU57510 is also mapped as adularia 2 (maroon) in LWIR (SAM) map. For sample AU57522 and AU57540, quartz veins, as identified from TIMA images, are rarely classified as quartz veins in LWIR (SAM) maps. Instead, the veins are classified as quartz\_calcite veins. The same vein patterns are also observed in wavelength maps, which appear dark, suggesting shallow depth of emissivity minima. LWIR mapped calcite in all the four samples presented in *figure3.15*. However, only sample AU57510, had a matching, spatial distribution of calcite with its corresponding TIMA map while the other three TIMA maps show no sign of calcite. Moreover, various minerals such as clinocllore, nontronite, pyrite, chalcopyrite present in TIMA maps are absent in LWIR maps for all the samples displayed in *figure3.15*.

Misrepresentation of minerals was highly noticed in sample AU57545 (*figure3.15*), where SAM mapped most pixels as adularia1 (red) (*figure3.16a*). According to TIMA and XRD, no adularia is present and there is a significant amount of quartz and rare albite (*appendix3* and *4*). This is in agreement with spectral characteristics of the pixels, which shows mixed spectra with no resemblance to the adularia spectrum. The mixed spectrum, as shown in *figure3.16b*, shows strong bands of quartz highlighted by its emissivity peak at 8629nm. ISMA results appear to agree with the spectral behavior of the mixed pixel, where quartz contains ~40% abundance per pixel (*figure3.16b*). Also, from the RGB of ISMA results, quartz (green) dominates this rock sample with rare albite (blue), which agrees with TIMA and XRD for this particular sample.

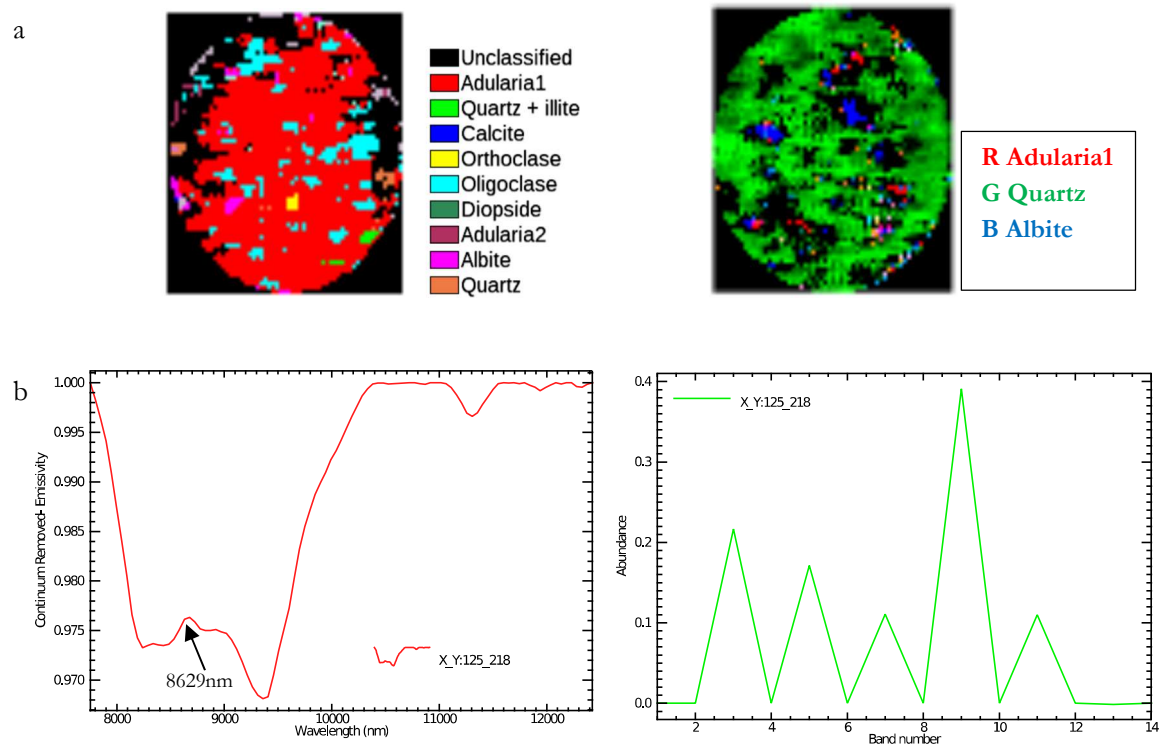
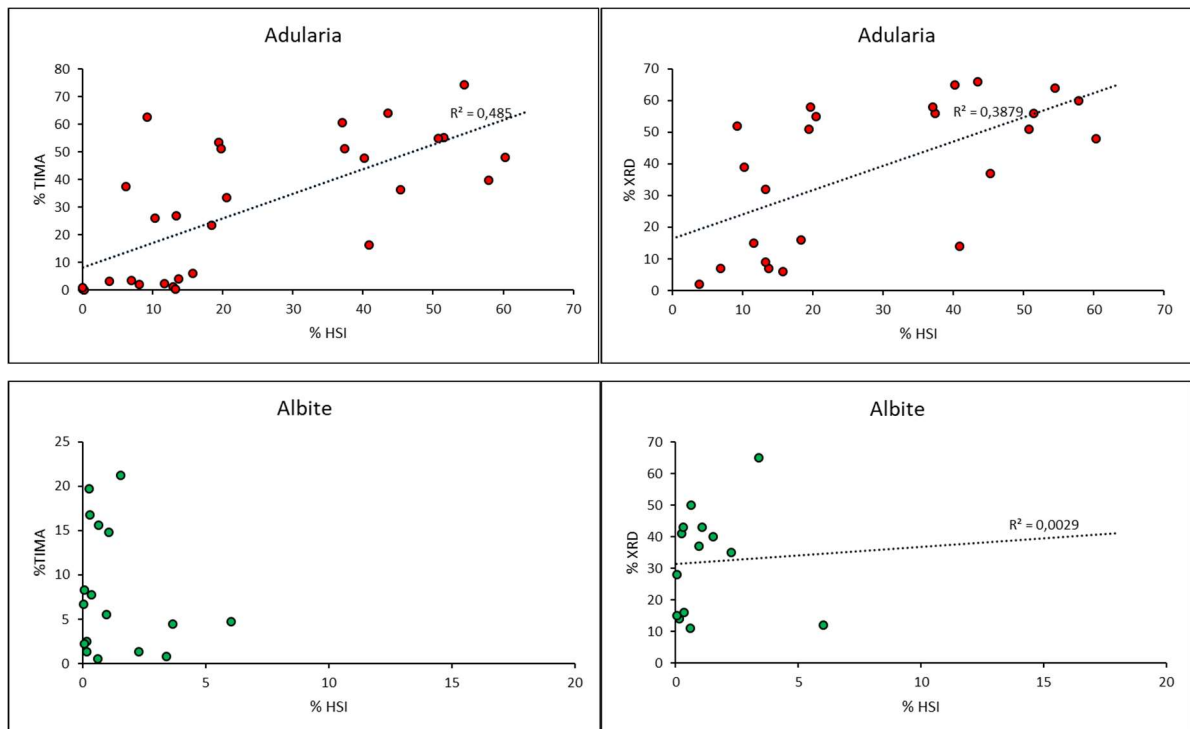


Figure 3.16: a) SAM classified image(right) and ISMA results for sample AU57545 b) their corresponding spectra (right) and abundance profile(left)

### 3.6.2. Quantitative comparison: HSI, TIMA and XRD

Mineral percentage estimates used in the quantitative analysis are described in appendix 1,2 and 3. It includes mineral abundance determined from SAM mineral maps, TIMA and XRD results. *Figure 3.17* shows mineral abundance plots for samples that were common in all datasets. These plots were of TIMA versus HSI(LWIR) and XRD versus HSI(LWIR) for adularia, quartz, albite and calcite. The calculated correlation coefficient based on the best fit (linear line) for the few selected minerals is displayed within the plots as R-squared value. Generally, the correlation coefficient of the selected minerals in the different datasets was lower than  $\sim 0.5$ . Furthermore, albite shows less than 0.1 coefficient of correlation.

Among the selected minerals, adularia had a close match in the mineralogical content compared to other minerals with an R-squared value of 0.485 (TIMA) and 0.3879 (XRD), as shown in *figure 3.17*. Again, plots show a lower percentage of classified minerals for various samples in LWIR spectroscopy compared to other methods for albite, quartz, and calcite. For albite, most samples had lower mineral percentage compared to the other methods. There is no clear trend for quartz. Generally, quartz is present only in small amounts, but it appears to be abundant in LWIR mineral maps. Quartz is overestimated for most samples compared to other methods showing an increase in LWIR (HSI) mineral maps. Calcite is present in most sample images (HSI) but with a very low percentage while it appears in a high percentage in very few samples for TIMA and XRD dataset.



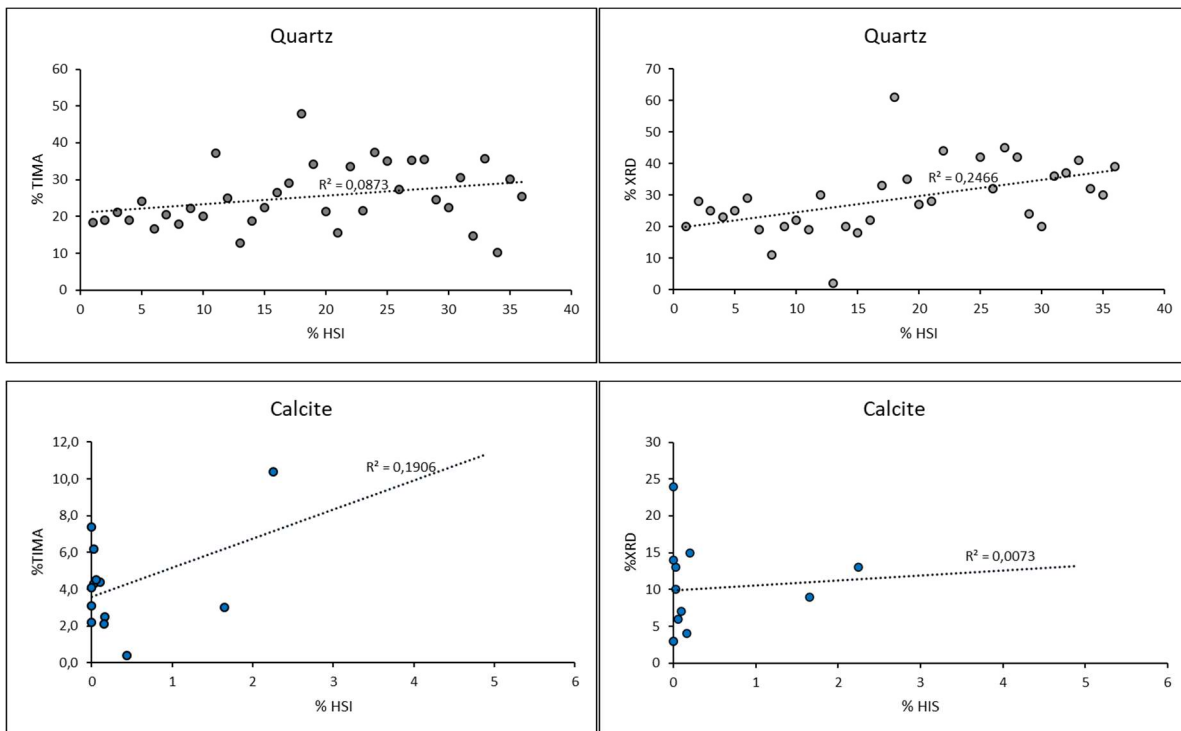


Figure 3.17: Cross plots of HSI(LWIR) versus TIMA and XRD mineral percentage estimates for adularia, albite quartz and calcite

### 3.7. Association of adularia with other minerals

Determination of minerals associated with adularia was determined by analyzing mineral percentage estimates as well as spatial distribution of minerals for the selected adularia-rich samples. *Figure 3.18* shows the distribution of adularia in various sample images with a decreasing percentage of adularia (to the right). The occurrence of adularia and albite displays a contrary relationship; adularia percentage estimate increases with a decrease of albite percentage estimate and vice versa is true.

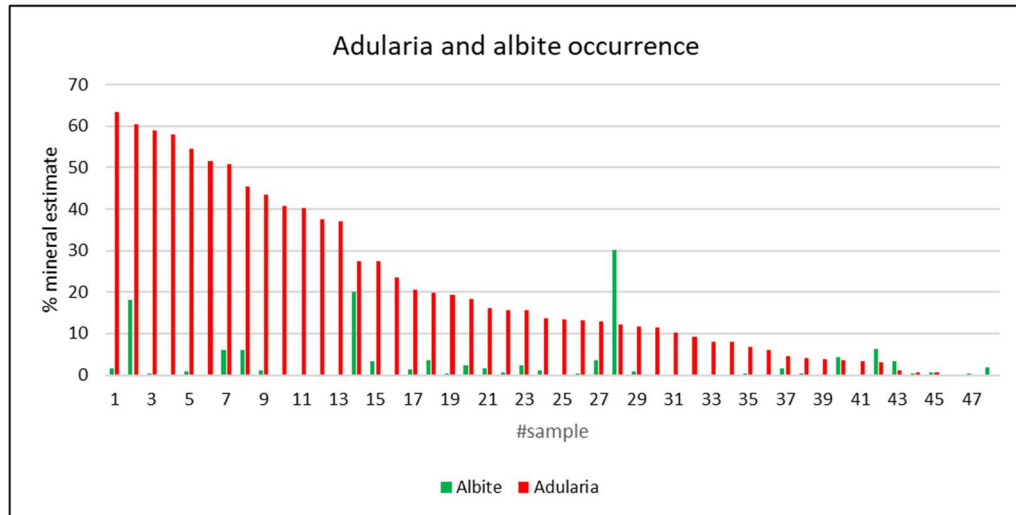


Figure 3.18: Adularia versus albite occurrence in the decreasing order of adularia content (to the right)

The first ten samples (>30%adularia) in figure3.18 were selected. Table 3.4 displays the selected samples, which are considered to be adularia rich based on the assumption that samples with >30% adularia are adularia-rich samples. Ten samples with the highest percentage of adularia common to both dataset, LWIR and TIMA were selected. Adularia dominates all the selected samples relative to other identified minerals. Quartz is present in all the selected samples as pure and in mineral mixtures. Albite and anorthoclase appear to be abundant in sample AU 57555. Calcite is also abundant in sample 57522 relative to other minerals. Diopside mineral is present in an insignificant amount (2.73%) in sample AU57493 but is considered to be important in a mineral assemblage of unaltered/weakly altered rocks.

No.	AU#	Mineral Abundances (%)										
		Adularia	Qz	Chalc	Qz-l	Qz_cal	Cal	Or	Olg	Di	Albite	Ano
1	57555	60.29	0.33	0.16	0.26	1.24		0.46	1.43		18.02	15.97
2	57522	57.9				8.45	4.91				0.16	
3	57598	54.45	0.03			0.94			17.57		0.94	0.13
4	57556	51.5	0.03			1.82	0.79		14.57		0.09	
5	57567	50.74				6.29	0.09		19.68		6.07	
6	57493	45.3				3.76	2.24	3.42	3.32	2.44	6.03	2.74
7	57488	43.52	8.22	0.46		0.83	0.96	0.43	0.4	0.6	1.03	0.03
8	57541	40.22	3.02	0.19	4.6			0	14.38	0.13	0.25	0.38
9	57595	37.42	0.11			0.42	0.07					
10	57602	37.03	18.12			1.45						0.03

Table 3.4: LWIR mineral percentage estimates for the ten selected adularia-rich samples with >30% adularia

Based on mineral percentage estimates and spatial distribution of minerals obtained from LWIR maps, a list of minerals that commonly occur with adularia were determined. *Table 3.5* present dominant minerals in adularia rich samples as well as spatially associated minerals based on observation of their corresponding minerals maps. Commonly associated hydrothermal minerals with the occurrence of adularia are highlighted by pale yellow colour as seen in *table 3.5*, which includes quartz, calcite and albite.

Sample code (AU#)	LWIR mineral estimates (decreasing % to the right)	LWIR minerals maps (Spatial association)
57555	Albite, anorthoclase, quartz	Anorthoclase, quartz, albite
57522	Quartz, calcite	Quartz
57598	Oligoclase, quartz, albite	Oligoclase
57556	Oligoclase, quartz, albite	Oligoclase
57567	Oligoclase, quartz, albite	Quartz, oligoclase
57493	Albite, quartz, anorthoclase, oligoclase, diopside	Anorthoclase, calcite, diopside
57488	Quartz, calcite, albite, diopside	Quartz
57541	Orthoclase, quartz	-
57595	Quartz, calcite	-
57602	Quartz, calcite	Quartz

Table 3.5: Common minerals associated with the occurrence of adularia from LWIR classified results

## 4. DISCUSSION

### 4.1. Methods

Hyperspectral image of the rock plugs was acquired in the longwave infrared (LWIR) of 7704.44nm to 12571.9nm wavelength range. Due to noisy bands, the spectral range was reduced to 7753nm-12400nm through spectral subsetting. The use of this wavelength range influenced the distinction of the identified minerals. This is because of wavelengths beyond 12000nm exhibit secondary features that could be useful to identify and confirm the presence of minerals such as quartz, albite, or mineral mixtures (Ruff, 1998).

The acquired hyperspectral image has shown an exponential increase of reflectance values from ~10500nm to 12400nm, as observed in an image spectrum presented in *figure3.2*. This may have attributed to the self-emission effect when the rock gets exposed to light. Due to the slow scanning process, the rock gets ample time to heat up and emit energy. Therefore, the total recorded reflected energy may have incorporated the emitted energy as well. This has affected the position of diagnostic features and to reduce the effect, continuum removal was used to determine the exact wavelength position of diagnostic features, particularly in endmember identification. However, an improved acquisition method would be useful to account for this effect completely.

Four algorithms were used to process images; wavelength mapper and PCA for endmember collection, SAM and ISMA for mineral mapping. Wavelength mapper facilitated endmember extraction, highlighting emissivity minima, which are typical diagnostics features of mineral present in the investigated dataset. However, endmember picking became difficult from wavelength maps, particularly for spectral signatures that exhibit emissivity minima at the same wavelength position but differs in shape and wavelength position of their emissivity peaks. This was demonstrated in the wavelength map of sample AU57491 (*figure3.5*), where different spectral features at the same wavelength position were highlighted by blue colour despite their differences in shape and emissivity peaks. PCA was also used to facilitate endmember extraction. For example, albite and adularia1 endmembers with their deepest feature at ~9554nm were differentiated by different colours in PCA results. The use of PCA and wavelength mapper has, therefore, complemented each other in the endmember collection.

SAM classification method depends on the SAM algorithm and endmember list; however, the quality of the output map highly depends on the user. This was demonstrated in the SAM classification algorithm applied to the pre-processed LWIR images. This method is straight forward; however, user-interaction is necessary for the attainment of realistic results. The use of a single threshold value (~0.05radians) for all endmembers led to the misrepresentation of pixels. Most misrepresented pixels were mixed and their spectral signatures were absent in the endmember list. Therefore, multiple values for different endmembers were used. The

use of multiple threshold values is user-biased because the selection of threshold values depend on histogram inspection and random pixel inspection.

Prior to the quantification of SAM classification results, duplicate mineral classes were dealt with, i.e., adularia, as described in section 3.5.1. However, mixed classes were not accounted for because the proportion of the mineral constituent of that mainly mixed spectra is unknown. However, their presence influenced the quantification of minerals for SAM classified images. *Figure 3.12*, where an assumption was made and 50% of, for example, quartz\_illite was added to quartz mineral estimate. Distribution of quartz minerals dramatically changes especially for few samples that had less than 40% shoot up to ~60% which resembles is observed with most samples that had low values of

Mixture analysis (ISMA) was also performed to account for the percentage estimates of mixed pixels for comparative studies with TIMA and XRD data. ISMA was used to investigate fractional mineral abundances of such pixels. This method highly depends on the purity of endmembers and this can be a disadvantage to the analysis given the presence of mineral mixtures. The results obtained were unrealistic, displaying both negative and positive abundance values. The presence of negative values made data interpretation difficult for the whole sample image. However, ISMA analysis results demonstrated the possibility of determining fractional mineral abundance per pixel as it retains endmembers that have spectral information relevant to a given mixture. This was observed in few pixels that had positive fractional abundance summed up to ~1, and their spectral signatures were characterized by subtle diagnostic features representing their mineral constituents per pixel (*figure3.13*). This suggests the use of ISMA technique to study spectral behaviour of mineral mixtures using an abundance image.

## **4.2. Spectral characteristics of feldspars and other minerals**

Feldspar minerals are spectrally characterized by diagnostic features within ~8100- 10500nm wavelength range. In this study, various feldspar minerals were identified based on their distinct spectral signature. The identified feldspars include plagioclases (albite and oligoclase) and alkali feldspars (adularia, orthoclase and anorthoclase). Other identified minerals were quartz, calcite, chalcedony, quartz\_illite and quartz\_calcite.

Compositional variations have shown a significant influence on band position of spectral features, as shown in section 3.4.1. For example, adularia exhibit features within 8100nm- 10500nm related to Si-O-Al bond within its structural framework while calcite exhibit carbonate related feature at 11300nm. Symmetry, width and depth of spectral features were useful in the distinction of identified minerals beside band position. Spectral features in plagioclases appear broad and shallow compared to spectral features in alkali feldspars, which appears sharp and deep. Also, albite has multiple features at 8726nm, 9213nm, 9554nm and 9797nm (*figure3.6a*). An anorthoclase spectrum also appears to have an asymmetrical shape with its second feature at

9602nm being deep compared to the first feature at 8434nm. This is in comparison to adularia1 with almost two symmetrical features at 8434nm and 9554nm. Likewise, emissivity spectra of quartz and chalcedony are both asymmetrical with their corresponding spectral features at 8239nm, 9310nm and 8385nm, 9262nm, respectively. Their difference was mainly highlighted by band position and shape of emissivity minima where chalcedony had smooth/round features (*figure3.8c*) relative to quartz, which had sharp emissivity minima (*figure3.8a*).

Features within 8400-11000nm wavelength range characterizes feldspar minerals. These features result from Si-O and Si-Si and Si-Al stretching modes. Pure cation (Ca, Na, K) stretching modes cause features beyond ~18500nm. However, its effect is highlighted in the reststrahlen band as well, whereas, for albite (Sodic feldspar), well defined multiple features reflect the presence of sodium. The intensity of these diagnostic features decreases with an increase in calcium content. In this study, the presence of calcium was highlighted by weak and poorly defined features of albite, as seen in *figure3.6*. This suggests that albite present in this dataset is Ca-rich.

Deviations between image and reference spectra, as described in section 3.4.1 and 3.4.2, are due to variability in the composition of minerals. The identified mineral spectra had minor shifts of their emissivity minima while maintaining their peak at the same wavelength position, for example, of oligoclase and quartz. The image spectrum of oligoclase had a shift of its spectral features towards shorter wavelengths by ~48nm and 97nm from its corresponding reference spectrum, maintaining its peak at 9310nm. The first and second spectral feature of quartz appears to shift to shorter wavelength by ~150nm and longer wavelength by 110nm, respectively maintaining its peak at 8629nm. Mineral mixtures may have contributed to this as observed in the oligoclase spectrum (*figure3.6*) and quartz spectrum (*figure3.8a*), where a subtle carbonate related feature is highlighted at ~11300nm. This has demonstrated the presence of mineral mixtures as well as suggests that the emissivity peak (the Christiansen feature) can be a useful indication of mineralogy, as suggested by Salisbury et al., (1991), especially when in a mineral mixture.

Salisbury et al., (1991) showed that minerals such as quartz persist in their respective reststrahlen bands despite changes observed in the intensity or shape of the spectra. In this study, the presence of minerals with persistent features such as quartz influenced the detection of other minerals as well as affected balance in mineral quantification. This is because quartz bands are so strong and when present even in small amounts, they tend to be more prominent in most pixels, including mixed pixel, as observed in *figure3.8*. This may obscure spectral features of other minerals that are present in a small amount. However, the persistent features such as quartz emissivity peak at 8629nm made identification of quartz easy even when in a mineral mixture.

### 4.3. LWIR mapping of feldspars and associated minerals

Mineral mixtures had a significant influence not only in mineral identification but also in mineral mapping and quantification. Most minerals expected in these rock samples based on TIMA results were not mapped by LWIR spectroscopy. Such minerals are clay minerals, clinocllore, chamosite, chlorite, montmorillonite, hornblende and anorthite. This may have attributed to the mineral mixtures or insignificant amount of these minerals present in the dataset, given the low spatial resolution of LWIR maps (400 $\mu$ m) relative to high spatial resolution of TIMA maps (2-5 $\mu$ m). Based on TIMA results, minerals such as smectite, Kaolinite and hornblende were present in less than 1% and there was no evidence of their presence in LWIR mineral maps. Clay minerals such as illite were present in a significant amount of up to 35% in TIMA results but were only detected as a mixture of quartz and illite in LWIR data. The Illite\_quartz spectrum showed an overlap of absorption features diagnostic for quartz and illite. Given these circumstances, SWIR could be an alternative wavelength range to identify and confirm the presence of, for example, clay minerals, which are active in SWIR spectral range.

Only six LWIR mineral maps had clear spatial patterns that could easily be compared with TIMA maps. Mostly, this was due to the presence of a large number of unclassified pixels observed in most sample images. Only 26 out of the 42 sample images were classified by atleast 50% of the pixels. For those few samples, patterns look similar despite their differences in mineral content, which suggests misrepresentation of minerals. Misrepresentation of minerals resulted in underestimation and overestimation of minerals from LWIR mineral maps (SAM classified results), as demonstrated in *figure3.16*. This was observed in the comparative analysis between LWIR, TIMA and XRD data. Albite classified pixels in TIMA were classified as anorthoclase and oligoclase in LWIR maps. Albite has multiple diagnostic features within a 9400nm-9900nm wavelength range. These features distinguish it from anorthoclase, adularia, and oligoclase. As discussed in section 4.2, the weak and less pronounced features in albite almost resemble anorthoclase and oligoclase spectral signature in terms of band position. This explains the confusion between albite, anorthoclase and oligoclase in SAM mineral mapping.

Adularia dominates most samples, while other feldspars such as albite, only dominate few samples. Adularia dominates most rock samples, as shown in both LWIR and TIMA mineralogical estimates (see *Appendix 1 and 2*). At least in 22 samples, the amount of adularia exceeds that of other identified minerals such as albite and quartz. However, adularia is higher than 30% in mineralogical estimates in LWIR data for only 27% of the rock samples (*figure3.18*). Based on LWIR results, the percentage estimate for albite is higher than 18% of the pixels in only three samples AU57510, AU57540 and AU57555. Among the three, only AU57510 had a match with TIMA and XRD data. The other two samples show no sign of albite. Despite the less correlated results, especially for albite, the relationship between adularia and albite remains to be contrary where adularia is high whenever albite is low. This information is useful in permeability studies in geothermal systems.

Comparison between LWIR, TIMA and XRD data on identification and mapping of the minerals in the rock samples shows that LWIR data take advantage, particularly in the identification of minerals such as silica minerals. Spectral information reported the presence of chalcedony at the periphery of some quartz\_calcite veins. This is in agreement with a study by Simpson et al. (2019), who documented the presence of quartz, calcite, chalcedony and pyrite occurrence to mainly occur in veins. However, TIMA could not distinguish different forms of silica and mapped all as quartz. This may have been attributed to the mapping algorithm in TIMA, which is based on chemical composition. Given, both Chalcedony and quartz are silica minerals with the same chemical formula of  $\text{Si}_2\text{O}$ .

LWIR maps have demonstrated the ability to detect calcite. However, calcite spectra present in this dataset suggest the presence of another mineral other than calcite, which has contributed to subtle features at 8288nm, 9268nm, and 9748nm that are non-calcite related (*figure3.8g*). SAM algorithm classifies the image based on spectral fit of the specified spectral range. Therefore pixels that had features similar to the ones at shorter wavelengths were as well classified as calcite despite the absence of a calcite-related feature at  $\sim 11300\text{nm}$ . This observation was made based on a random pixel inspection. This explains the identified calcite present in more than 50% of the rock samples. This is not in agreement with a study done by Simpson et al., (2019), who reported the presence of calcite in only 33% of the rock samples using TIMA. However, calcite percentage estimate for 50% of the LWIR image samples is underestimated relative to TIMA results (*figure3.17*). The underestimation might be attributed to the mineral mixtures that were not accounted for in SAM mineral quantification. For example, a diagnostic feature for calcite at 11350nm present in oligoclase and quartz\_calcite spectra was not accounted for during mineral quantification.

LWIR and TIMA had relatively close mineral estimates compared to XRD. For example, calcite is significant, ranging up to 24% in XRD. However, it is present up to 2% and 10% in LWIR and TIMA. This may be attributed to the difference observed in the mode of measurement. XRD measurements took place on powdered rock samples. In comparison to LWIR and TIMA, whose measurements were done on the same surface of the investigated rock plugs of 1inch diameter.

Generally, LWIR results show similarity in mineral abundances relative to other datasets, particularly for adularia (*figure3.17*). This is demonstrated by the coefficient of correlation between LWIR, TIMA and XRD relative mineral abundances, which was  $\sim 0.5$  for adularia. Other minerals, such as albite, had a correlation coefficient of up 0.1 for albite. This suggests that mapping of minerals by different techniques correlated well with adularia relative to other minerals.

Pyrite is a common hydrothermal alteration mineral present in most vein-rich rock samples. Pyrite was identified through visual observations of the rock samples as it appears in brass-yellow with a metallic luster

on rock surfaces and from TIMA maps. Pyrite was distributed throughout the samples, particularly around veins. TIMA maps mapped pyrite, which was in agreement with the rock samples. Pyrite has no spectral absorption features; hence was not determined by LWIR.

TIMA results were used to facilitate endmember collection and assess the methodological approach used, i.e., mineral mapping. However, the use of TIMA had an influence on adularia endmember collection as well as quantification of adularia. Given the limited number of studies on adularia, TIMA minerals maps were used to pinpoint adularia-rich samples that were used to extract adularia endmembers from LWIR images. This was done despite that TIMA maps were used in comparative analysis to validate LWIR data. The endmember collection presents two adularia endmembers, adularia1 and adularia2, that were selected based on the TIMA maps. Wavelength mapping results show that adularia2 is a mixture of a feldspar mineral and quartz, while in ISMA results, adularia2 appears to be a mixture of orthoclase and quartz. This suggests further studies of adularia in order to understand spectral behavior of adularia before applying it to mixed samples.

#### **4.4. Hydrothermal alteration**

This study used data from Karangahake low sulfidation Au-Ag epithermal system. Rock samples are from vein rich area based on alteration zones, as suggested by Simpson et al., (2019). No other alkali feldspars were identified apart from adularia/orthoclase and anorthoclase. This is not in agreement with the previously identified K-feldspar from the rock samples collected from Karangahake, where the only alkali feldspar documented was adularia (Simpson et al., 2019). However, anorthoclase is not strictly defined as alkali feldspar due to its composition (refer to figure1.1). Still, a common alteration mineral in the Karangahake Au-Ag epithermal system remains to be adularia, which is in significant amount in LWIR, TIMA and XRD data. This suggest dominance of K-metasomatism alteration process in epithermal veins where the formation of K-bearing minerals and loss of Ca and Na is common.

Given the high percentage of unclassified pixels (~ more than 50% of the pixels observed in 16 sample images), hydrothermal alteration minerals that are spatially associated with adularia are insufficient to establish mineral assemblage that would significantly be used to identify adularia-rich areas. LWIR mineral maps show that hydrothermal minerals; quartz, calcite and albite are spatially associated with the occurrence of adularia. Quartz is present in significant amounts in all adularia rich samples in comparison to albite and calcite, which are present in an insignificant amount in most of those samples. Minerals such as quartz are common in several minerals assemblages in different geological environments. Therefore, a combination of these hydrothermal minerals; quartz, calcite and albite are not sufficient enough to be used as a mineral assemblage to identify adularia-rich areas. However, these hydrothermal minerals can be used to identify vein rich areas.

Calcite and quartz are mapped veins and quartz at the periphery of the veins in LWIR images. This suggests different episodes of deposition, which is calcite came later relative to the occurrence of quartz mineral. This is in agreement with the study done by Simpson et al., (2019), which documented calcite as an alteration mineral that formed in the late-stage cavity in some quartz veins.

In summary, the results of this analysis demonstrate the importance of LWIR imaging spectroscopy in understanding feldspar minerals from the investigated rock plugs. It enabled the identification and discrimination of various feldspar and other associated minerals such as adularia, albite and quartz. These are important hydrothermal minerals in a geothermal system. The identified minerals were validated with documented minerals from a previous study by Simpson et al., (2019). However, this technique is limited to the detection of minerals that were either present in complex mineral mixtures or present in an insignificant amount or inactive in the LWIR spectral range.

## 5. CONCLUSION AND RECOMMENDATIONS

The primary objective of this study was to assess whether LWIR imaging spectroscopy can identify and distinguish adularia from albite and other feldspar minerals. Results and discussion on the spectral study together with TIMA and XRD data of the rock plugs from Karangahake epithermal system has led to the following conclusions;

- LWIR imaging spectroscopy can identify various feldspar minerals, as discussed above. Expected feldspar minerals that were not detected by LWIR were present in an insignificant amount based on the relative abundance of minerals derived from TIMA data of the same rock plugs. This may have attributed to the fact that such minerals were not spectrally prominent. Also, the presence of minerals with strong bands such as quartz may have obscured spectral features for such minerals, especially their emissivity peaks (an indication of mineralogy), which appears wide and flat for most mixed spectra.
- Adularia has a distinct spectral signature, which can easily be distinguished from other minerals, for example, from albite by subtle variations in intensity, wavelength position, symmetry, width and number of diagnostic spectral features. In mineral mixtures, especially feldspar to feldspar mixture, adularia can spectrally and spatially be confused with other feldspar minerals given their broad features within ~8100nm to 10000nm spectral range. However, emissivity peaks that persist at the same wavelength position as in reference mineral spectra can be used to indicate mineralogy of various minerals even when in mineral mixtures. Also, albite present in these rock plugs tends to have calcium, thus spectrally confused with oligoclase.
- There is a possibility of using the relationship of adularia and albite in future permeability studies in geothermal systems. This is based on spectral signature for adularia, which is distinct enough from albite and adularia versus albite occurrence relationship, which is inverse. However, when mixed or when albite is calcium-rich, there is a possibility of spectral confusion between the two minerals. In addition, it is crucial to understand their occurrence phases as well, which would have been possible with LWIR spectroscopy if mineral patterns were clear enough to extract information on adularia-albite mineral phases.
- Based on LWIR mineral maps, the investigated rock samples are altered due to the presence of alteration minerals such as adularia, calcite, albite, etc. Hydrothermal minerals; quartz, calcite and albite are spatially associated with the occurrence of adularia. Quartz is present in a significant amount compared to other hydrothermal alteration minerals, i.e., calcite and albite. However,

minerals such as quartz are common in other geological environments and given high percentages of unclassified pixels ( $\sim >50\%$ ) observed in 16 sample images, it is inconclusive that these are the only hydrothermal minerals present in this dataset. Therefore, a combination of these hydrothermal minerals is not sufficient enough to be used as a mineral assemblage to identify adularia-rich areas.

- From the results of algorithms used in this study, wavelength maps give an overview of the mineral patterns; however, not all spectral information can be displayed based on emissivity peaks and shape of the spectral features. PCA gives an overview of the number of uncorrelated bands from the sample image. SAM is a straight forward technique; however, the quality of output maps requires user intervention. ISMA technique provides an alternative approach in understanding spectral behavior of mixed pixels based on the abundance images due to the realistic results obtained for specific pixels. However, it is not likely to provide realistic results for the whole sample image as the results of negative abundance values. The approach used in this study has demonstrated usefulness of various methods. Individual methods provided unique information that complemented each other.
- The performance of LWIR imaging spectroscopy relative to TIMA and XRD technique was evaluated based on comparative analysis. LWIR, XRD, and TIMA perform differently from sample preparation to data acquisition to data processing. LWIR and TIMA were expected to highly correlate given measurements were done on the same rock surfaces. That was not the case, given a poor correlation coefficient of up to 0.5 for various minerals. This may have been attributed to an insignificant amount of minerals whose spectral features were hardly pronounced, mineral mixtures, differences in modes of measurement and spatial resolution. However, there were common minerals mapped by all three techniques despite their differences in mineral proportion and spatial distribution.
- TIMA was used not only used to assess the LWIR performance on rock plugs but also to facilitate the endmember collection process in particular for adularia. This had an influence on adularia endmember as well as quantification of adularia mineral. Therefore, analysis of secondary features can be used to confirm whether adularia2 a mineral mixture.

Based on the results, the following are recommended;

- This study used LWIR spectral range of ~8000nm -12000nm. Various minerals were identified; however, not all minerals were identified and due to mineral mixtures, it was challenging to identify complex mixed spectra. Therefore, an optimal spectral range is highly recommended in the identification and distinction of minerals present in the investigated dataset. SWIR spectral range can be useful in targeting other associated minerals active in this specific range (e.g., muscovite, kaolinite, chlorite, calcite) and confirm the presence of mixtures of, for example, clay minerals. LWIR wavelengths beyond 12000nm can also be useful to identify and confirm the presence of, for example, quartz and feldspars in mineral mixtures.
- ISMA worked well for specific pixels for LWIR data. Therefore, research on this technique is strongly recommended, particularly on LWIR images. This is because the ISMA technique proved to be reliable in various studies on SWIR data, such as a study by Rogge et al. (2006) and Cecilia & Acosta, (2017). Based on the spectral results, as discussed in section 4.3, adularia2 is yet to be well understood, whether it is adularia or a mineral mixture. Therefore, further research on adularia is recommended to better understand the behavior of adularia in spectroscopy for reference purposes. This would also assure the possibility of having pure endmembers for a successful spectral mixture analysis.

## LIST OF REFERENCES

---

- Abera, M. G., Hecker, C., & Bakker, W. (2018). *Characterization of Rock Samples Using Swir-Lwir Hyperspectral Imaging techniques- an Example of the High Epithermal system of Rodaquilar, Southeast Spain. MSc Thesis.* University of Twente, Enschede.
- Baptiste, N., & Chapuis, R. P. (2015). What maximum permeability can be measured with a monitoring well? *Engineering Geology*, *184*, 111–118. <https://doi.org/10.1016/j.enggeo.2014.11.006>
- Bogie, I., & Lawless, J. (2000). Application of mineral deposit concepts to geothermal exploration. In KingstonMorrison (Ed.), *World Geothermal Congress*. Kyushu-Tohoku.
- Borengaser, William, H. S., Watkins R., & Michael T. Eismann. (2012). *Hyperspectral Remote Sensing. Taylor & Francis series in remote sensing applications* (Vol. 30). <https://doi.org/10.1117/3.899758>
- Browne, P. R. L. (1970). Hydrothermal alteration as an aid in investigating geothermal fields. *Geothermics*, *2*(2), 564–570. [https://doi.org/10.1016/0375-6505\(70\)90057-X](https://doi.org/10.1016/0375-6505(70)90057-X)
- Browne, P. R. L., & Ellis, A. J. (1970). The Ohaki-Broadlands hydrothermal area, New Zealand; mineralogy and related geochemistry. *American Journal of Science*, *269*(2), 97–131. <https://doi.org/10.2475/ajs.269.2.97>
- Cerny, P., & Chapman, R. (1984). Paragenesis, chemistry and structural state of adularia from granitic pegmatites. *Bulletin de Mineralogie*, *107*(3–4), 369–384. <https://doi.org/10.3406/bulmi.1984.7767>
- Christensen, P. R., Bandfield, J. L., Hamilton, V. E., Howard, D. A., Lane, M. D., Piatek, J. L., ... Stefanov, W. L. (2000). A thermal emission spectral library of rock-forming minerals. *Journal of Geophysical Research E: Planets*, *105*(E4), 9735–9739. <https://doi.org/10.1029/1998JE000624>
- Contreras, I. C., Hecker, C., & van der Meer, F. (2015). Mapping Epithermal Alteration Mineralogy With High Spatial Resolution Hyperspectral Imaging of Rock Samples. *GRSG Conference*, 123–128.
- Dietrich, R. . (2018, August 9). Feldspar | Properties, Uses, Types, & Facts | Britannica. Retrieved May 25, 2020, from <https://www.britannica.com/science/feldspar>
- Fagbohun, B. J. (2015). *Combining Dominant Spectral Features in Airbone SWIR and TIR Imagery For Mineralogical Mapping.* University of Twente.
- Feely, K. C., & Christensen, P. R. (1999). Quantitative compositional analysis using thermal emission spectroscopy: Application to igneous and metamorphic rocks. *Journal of Geophysical Research*, *104*(October), 169.
- Field, R. M., Rafik, B., & Kamel, B. (2017). Prediction of permeability and porosity from well log data using the nonparametric regression with multivariate analysis and neural network , Hassi R'Mel Field, Algeria. *Egyptian Journal of Petroleum*, *26*(3), 763–778. <https://doi.org/10.1016/j.ejpe.2016.10.013>
- Graham R. Hunt, & John W. Salisbury. (1970). Visible and Near Infrared Spectra of Minerals and Rocks: I Silicate Minerals. *Modern Geology*, *1*, 283–300.
- Green, A. A., Berman, M., Switzer, P., & Craig, M. D. (1988). A Transformation for Ordering Multispectral Data in Terms of Image Quality with Implications for Noise Removal. *IEEE*

- Transactions on Geoscience and Remote Sensing*, 26(1), 65–74. <https://doi.org/10.1109/36.3001>
- Hecker, C., der Meijde, M. van, & van der Meer, F. D. (2010). Thermal infrared spectroscopy on feldspars - Successes, limitations and their implications for remote sensing. *Earth-Science Reviews*. <https://doi.org/10.1016/j.earscirev.2010.07.005>
- Hecker, C., Dilles, J. H., Van der Meijde, M., & Van der Meer, F. D. (2012). Thermal infrared spectroscopy and partial least squares regression to determine mineral modes of granitoid rocks. *Geochemistry, Geophysics, Geosystems*, 13(3), 1–15. <https://doi.org/10.1029/2011GC004004>
- Hecker, C., van Ruitenbeek, F., Bakker, W., Fagbohun, B., Riley, D., van der Werf, H., & van der Meer, F. (2019). Mapping the wavelength position of mineral features in hyperspectral thermal infrared data. *Int J Appl Earth Obs Geoinformation*, 79(November 2018), 133–140. <https://doi.org/10.1016/j.jag.2019.02.013>
- Hecker, C., van Ruitenbeek, F., van der Werff, H., Bakker, W. H., Hewson, R., & van der Meer, F. (2019). Spectral absorption feature analysis for Finding Ore. *IEEE Geoscience and Remote Sensing Magazine*, 7(June 2019), 51–71. <https://doi.org/10.1109/MGRS.2019.2899193>
- Hochstein, M. P. (1988). Assessment and modelling of geothermal reservoirs (small utilization schemes). *Geothermics*, 17, 15–49. [https://doi.org/10.1016/0375-6505\(88\)90004-1](https://doi.org/10.1016/0375-6505(88)90004-1)
- Hochstein, M. P. (1990). Classification and assessment of geothermal resources. In M. H. Dickson & M. Fanelli (Eds.), *Small Geothermal resources - A guide to Development and Utilization* (pp. 31–59). Rome: UNITAR/UNDP Centre on small Energy Sources - Rome Italy.
- Hrstka, T., Gottlieb, P., Skála, R., Breiter, K., & Motl, D. (2018). Automated mineralogy and petrology – applications of TESCAN Integrated Mineral Analyzer (TIMA), 63, 47–63. <https://doi.org/10.3190/jgeosci.250>
- Hunt, G. (1977). Spectral signatures of particulate minerals. *Geophysics*, 42(2010), 501–513.
- Kerr, J. (2017). The Earth's Climate Balance and Consequences of Climate Change: Greenhouse gases. In *Introduction to energy and climate: Developing a sustainable environment* (First, pp. 53–76). CRC Press, Boca Raton. <https://doi.org/https://doi.org/10.1201/9781315151885>
- Kokaly, R. F., Clark, R. N., Swayze, G. A., Livo, E. K., Hoefen, T. M., Pearson, N. C., ... Klein, A. J. (2017). *USGS Spectral Library Version 7: U.S Geological Survey Data Series 1035*. <https://doi.org/10.1111/j.1467-9310.1980.tb01113.x>
- Kumar, A., Marcolli, C., & Peter, T. (2019). Ice nucleation activity of silicates and aluminosilicates in pure water and aqueous solutions-Part 3: Aluminosilicates. *Atmospheric Chemistry and Physics*, 19(9), 6059–6084. <https://doi.org/10.5194/acp-19-6059-2019>
- Lin, B., & Zhu, J. (2019). The role of renewable energy technological innovation on climate change: Empirical evidence from China. *Science of the Total Environment*, 659, 1505–1512. <https://doi.org/10.1016/j.scitotenv.2018.12.449>
- Pirajno, F. (2010). Hydrothermal Processes and Mineral Systems. In *Journal of Chemical Information and Modeling* (Second, Vol. 53, pp. 1689–1699). East Perth: Springer.

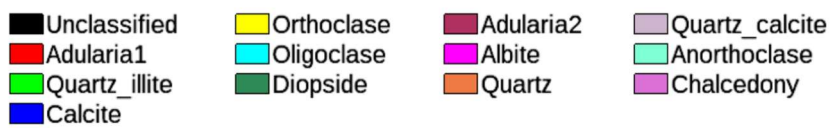
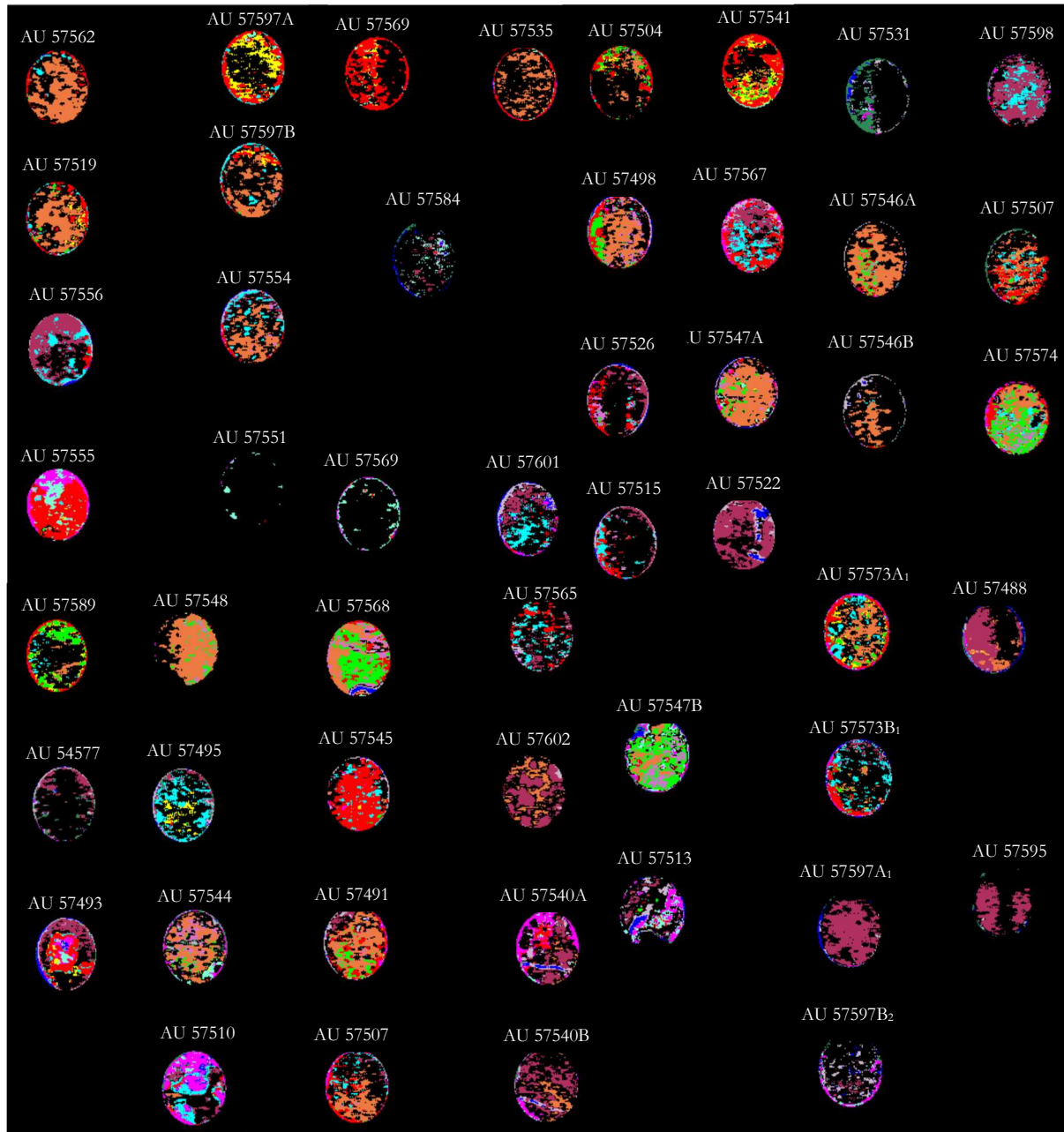
<https://doi.org/10.1017/CBO9781107415324.004>

- Reitze, M., Weber, I., Kroll, H., Morlok, A., Hiesin, H., & Helbert, J. (2019). Mid-Infrared spectroscopy of well defined alkali feldspar samples in preparation of metris observation. In *50th Lunar and Planetary Science Conference 2019* (pp. 1–2). Germany.
- Riley, D. N., & Hecker, C. A. (2013). Mineral Mapping with Airborne Hyperspectral Thermal Infrared Remote Sensing at Cuprite, Nevada, USA. In C. Kuenzer & S. Dech (Eds.), *Thermal Infrared remote sensing: Sensors, Methods, Applications* (17th ed., pp. 495–514). Springer. <https://doi.org/10.1007/978-94-007-6639-6>
- Rogge, D. M., Rivard, B., Jinkai, Z., & Jilu, F. (2006). Iterative spectral unmixing for optimizing per-pixel endmember sets. *IEEE Transactions on Geoscience and Remote Sensing*, *44*(12), 3725–3735. <https://doi.org/10.1109/TGRS.2006.881123>
- Ruff, S. (1998). *Quantitative thermal infrared emission spectroscopy applied to granitoid petrology*. PhD Thesis. Arizona state university.
- Salisbury, J. W., Walter, L. S., Vergo, N. V., & D’Aria, D. M. (1991). *Infrared (2.1 -25 $\mu$ m), Spectra of Minerals*. Baltimore and London: The John’s Hopkins University Press.
- Schodlok, M. C., Green, A., & Huntington, J. (2016). A reference library of thermal infrared mineral reflectance spectra for the HyLogger-3 drill core logging system. *Australian Journal of Earth Sciences*, *63*(8), 941–949. <https://doi.org/10.1080/08120099.2016.1234508>
- Simmons, S. F., & Browne, P. R. . (2000). Hydrothermal minerals and precious metals in the Broadlands-Ohaaki geothermal system: Implications for understanding low-sulfidation epithermal environments. *Economic Geology*, *95*(5), 971–999. <https://doi.org/10.2113/gsecongeo.95.5.971>
- Simpson, M. P., Gazley, M. F., Stuart, A. G. J., Pearce, M. A., Birchall, R., Chappell, D., ... Stevens, M. R. (2019). Hydrothermal alteration at the karangahake epithermal au-ag Deposit, Hauraki Goldfeld, New Zealand. *Economic Geology*, *114*(2), 243–273. <https://doi.org/10.5382/econgeo.2019.4630>
- Te Nijenhuis, J., Gateshki, M., & Fransen, M. J. (2009). Possibilities and limitations of X-ray diffraction using high-energy X-rays on a laboratory system. *Zeitschrift Fur Kristallographie, Supplement*, *30*(30), 163–169. <https://doi.org/10.1524/zksu.2009.0023>
- Thomson, J. L., & Salisbury, J. W. (1993). The mid-infrared reflectance of mineral mixtures (7-14  $\mu$ m). *Remote Sensing of Environment*, *45*(1), 1–13. [https://doi.org/10.1016/0034-4257\(93\)90077-B](https://doi.org/10.1016/0034-4257(93)90077-B)
- van der Meer, F., Hecker, C., van Ruitenbeek, F., van der Werff, H., de Wijkerslooth, C., & Wechsler, C. (2014). Geologic remote sensing for geothermal exploration: A review. *International Journal of Applied Earth Observation and Geoinformation*. <https://doi.org/10.1016/j.jag.2014.05.007>
- Yang, K., Huntington, J. F., & Browne, P. R. L. (2000). An infrared spectral reflectance study of hydrothermal alteration minerals from the Te Mihi sector of the Wairakei geothermal system , New Zealand. *Geothermics*, *29*(February 2018), 377–392. [https://doi.org/10.1016/S0375-6505\(00\)00004-3](https://doi.org/10.1016/S0375-6505(00)00004-3)

# 6. APPENDICES

## Appendix 1: SAM classified images

Below is a general overview of SAM classified images of 50 rock plugs, ~1inch diameter each.



**Appendix 2: Mineral estimates for LWIR maps**

A table below shows relative mineral abundances estimated from SAM classified images for 37 sample images.

AU#	Easting	Northing	Location	Mineral Abundances (%)												
				Unclassified	Adu1	Qz-I	Cal	Or	Olg	Di	Adu2	Ab	Qz	Qz_cal	Ano	Chalc
57488	2751631	6414877	Keillors crosscut	43.52	0.33		0.96	0.43	0.40	0.60	43.19	1.03	8.22	0.83	0.03	0.46
57491	2751625	6414879	Keillors crosscut	26.10	13.8	7.56	0.06	0.06	0.15		4.56	2.26	39.75	3.52	0.34	1.84
57493	2751618	6414884	Keillors crosscut	30.74	24.53		2.24	3.42	3.32	2.44	20.77	6.03		3.76	2.74	
57495	2751601	6414886	Keillors crosscut	55.91	0.39	0.23	0.35	6.92	23.61	3.03	6.51	0.26	0.06	2.64		0.10
57498	2751583	6414890	Keillors crosscut	30.73	11.4	9.73	0.16		0.44		0.22	0.96	35.46	1.12		9.79
57501	2751544	6414902	Keillors crosscut	54.71	40.85	0.03		2.60	0.12				0.06		1.56	0.06
57504	2751532	6414902	Keillors crosscut	67.43	13.3	5.97		2.23	0.48			0.15	9.32	0.15		0.97
57507	2751513	6414907	Keillors crosscut	53.13	11.09	0.13	0.03		6.03		2.61	1.07	24.03	1.32		0.57
57510	2751483	6414911	Keillors crosscut	28.50	3.66		4.15	0.21	15.49	3.15	8.62	30.23	1.21	2.78	1.69	0.30
57515	2751433	6414920	Keillors crosscut	72.85	9.06	0.10	0.10		6.94		6.65	0.63	0.32	1.62		1.74
57519	2751393	6414928	Keillors crosscut	39.66	9.92	2.15		3.03	1.96		0.35	0.06	41.81			1.04
57522	2751373	6414927	Keillors crosscut	28.58	0.13		4.91				57.77	0.16	0.00	8.45		
57526	2751357	6414933	Keillors crosscut	67.00	11.94	0.76	0.20		1.81		8.56	1.48	0.13	2.27		5.86
57531	2750829	6416565	Surface	73.65			2.68		0.03	16.46		1.78		3.82	1.58	
57535	2751125	6416128	Surface	68.75	3.82			0.13	0.13			0.03	26.16		0.98	
57540	2751390	6415735	Surface	38.88	8.44		2.36	0.00	0.00	0.03	19.09	20.07	1.68	6.94	2.51	
57541	2751395	6415705	Surface	36.83	40.22	4.60	0.00	14.38	0.13			0.25	3.02		0.38	0.19
57544	2753030	6415084	Surface	35.46	0.3	3.39	0.06	0.27	0.00	3.60	0.7	3.39	35.34	2.27	4.24	10.96
57545	2752941	6415115	Surface	22.36	62.75	0.49	0.03	0.31	9.22		0.49	1.54	0.89	1.54	0.31	0.06
57548	2752715	6415673	Surface	31.11	0.18	6.67	0.00	0.15		0.03		0.18	57.99		0.03	3.66
57551	2752330	6415754	Surface	97.02	0.06		0.00					0.30			2.61	
57554	2751400	6415595	Surface	47.30	3.38	0.12	0.15		10.83		4.67	0.15	29.80	1.35	0.09	2.15
57555	2751519	6415544	Surface	1.85	60.29	0.26		0.46	1.43			18.02	0.33	1.24	15.97	0.16
57556	2751636	6415555	Surface	31.20	3.28		0.79		14.57		48.22	0.09	0.03	1.82		
57562	2751662	6416279	Surface	38.17	6.12	0.15	0.21		2.59			0.03	52.40	0.06		0.27
57565	2751984	6416424	Surface	61.56	11.4		0.09		13.09		8.04	0.28	0.22	5.11	0.22	
57567	2752203	6416463	Surface	17.13	26.72		0.09		19.68		24.02	6.07		6.29		
57568	2752287	6416488	Surface	5.39	11.49	37.25	2.25	0.06	0.12			0.06	26.24	2.43	0.21	14.51
57569	2752432	6416529	Surface	91.60	0.54							0.60	0.00		7.19	0.06
57574	2750379	6416670	Surface	9.41	11.81	29.75		0.78	6.70	0.18	1.05	3.64	25.27	0.60	0.69	10.13
57577	2753788	6416450	Surface	77.86	0.03		0.44		0.03	5.79	13.23	0.37	0.16	2.02		0.06
57584	2751827	6414516	Surface	85.01	0.43		1.65			1.07	3.52	0.34	0.00	3.00	4.99	
57589	2751392	6415336	Surface	58.26	9.03	17.24		5.74	3.49	0.07	0.16	0.16	5.57			0.26
57595	2751133	6414706	Surface (rhyolite)	61.97			0.07				37.42		0.11	0.42		
57598	2751455	6415805	Surface	25.95	1.28				17.57		53.17	0.94	0.03	0.94	0.13	
57601	2751390	6415855	Surface	50.02	1.96		2.53		15.08	1.33	17.77	3.52		7.79		
57602	2751369	6415854	Surface	43.37	0.06						36.97		18.12	1.45	0.03	

AU# = Sample number

Easting and northing coordinates are New Zealand map grid

**Mineral abbreviations**

Ab = albite, Adu = adularia, Calc = calcite, Di = diopside, Qz-I = Quartz-Illite Olg= oligoclase, Qz = quartz Ano- anorthoclase chalc = chalcedony

### Appendix 3: Mineral estimates for TIMA mineral maps

A table below shows relative mineral abundances in percentage from 42 TIMA mineral maps. The mineral estimates was adapted from a study by Simpson et al., (2019).

AU#	Easting	Northing	Location	Mineral abundances (%)																																		
				Qz	Adl	Ab	ill	I-S	Sm	Chl	Ep	Kln	Cal	Py	Hm	Pl	Di	En	Hbl	Ap	Rt	Bt	Ilm	Ttn	Tmag	Unclassified												
57488	2751631	6414877	Keillors crosscut	18	64		2				0			2		4											1										9	
57491	2751625	6414879	Keillors crosscut	19	24	1	9	4	0	6						1						0	1														34	
57493	2751618	6414884	Keillors crosscut	21	36	5	1	2		7						2						0	1														25	
57495	2751601	6414886	Keillors crosscut	19	3	20	8	1		12						2												0									34	
57498	2751583	6414890	Keillors crosscut	24	2	6	4	2	2	7	0	1	3					11		0																	39	
57501	2751544	6414902	Keillors crosscut	17	16	7	8	5	0	4			0					2				0	1														39	
57504	2751532	6414902	Keillors crosscut	21	27	3	7	1		6						1						0	1														33	
57507	2751513	6414907	Keillors crosscut	18	4	15	7	4	1	8			4	0		3					0													0			35	
57510	2751483	6414911	Keillors crosscut	16	7	15	3	3	1	8	1		4	1		6				0							0						1			35		
57515	2751433	6414920	Keillors crosscut	22	6	16	5	4	0	7			4			2				0		0	0														32	
57519	2751393	6414928	Keillors crosscut	20	26	2	10	0		5			2									0	1														34	
57522	2751373	6414927	Keillors crosscut	37	40			5		0						3						0															14	
57526	2751357	6414933	Keillors crosscut	25	34		10			3						2						0	1														25	
57531	2750829	6416565	Surface	13	0					0			3					21	3	7									0					0			53	
57535	2751125	6416128	Surface	19	3	7	2	2	2	5				3	0	0	11										0								0		45	
57540	2751390	6415735	Surface	31	47		3	0		0						1											0										16	
57541	2751395	6415705	Surface	22	48		1	1	0	3																0	2										21	
57544	2753030	6415084	Surface	27		1	0	3	1	3			1	5			25			0														0			34	
57545	2752941	6415115	Surface	29		21	3	1	1	4			1	6			1					0															33	
57546	2752853	6415147	Surface	24			1	0	1	3	1			2			27			0																	40	
57547	2752822	6415400	Surface	30		10	5	3	1	5			2	6			2																0				36	
57548	2752715	6415673	Surface	48	0		35									2											0										15	
57551	2752330	6415754	Surface	34		17	9	2	0	5				2												0											29	
57554	2751400	6415595	Surface	21	2	1		2	1	6	2			2			20	3		0																	39	
57555	2751519	6415544	Surface	16	48		1	2		2																0	4											27
57556	2751636	6415555	Surface	34	55		0								2											0												9
57561	2751598	6416266	Surface	22	1	1		1	1	5	3			1			19	2		1						0			0								45	
57562	2751662	6416279	Surface	38	37		7									1										0												17
57565	2751984	6416424	Surface	35	53		2									1										0												8
57567	2752203	6416463	Surface	27	55		2			2						1										0	0											13
57568	2752287	6416488	Surface	35		8	12	1	0	4					10												0											27
57569	2752432	6416529	Surface	35		1	5	8	2	9	1			7	1											0												30
57573	2752934	6416526	Surface	25	1			1	1	3	0			1			26	5		1																	35	
57574	2750379	6416670	Surface	25	1	5		1	1	4			1	4			0	23							0													36
57577	2753788	6416450	Surface	23	0					6			1	0			0		30		1																	39
57584	2751827	6414516	Surface	31		8	23	1		4	1		3													0												30
57589	2751392	6415336	Surface	15	63		1			1	1			3												0												17
57595	2751133	6414706	Surface (rhyolite)	36	51		1						1																									12
57597	2751375	6415765	Surface	6	46		4	4		7						0										1	2											31
57598	2751455	6415805	Surface	10	74		0	0		2			0			1										0												11
57601	2751390	6415855	Surface	30	51		1	1		3						1										0												13
57602	2751369	6415854	Surface	25	61		2									1											0											12

AU# = Sample number

Easting and northing coordinates are New Zealand map grid

#### Mineral abbreviations

Ab = albite, Adl = adularia, Ap = apatite, Bt = biotite, Cal = calcite, Chl = chlorite, Di = diopside, En = enstatite, Ep = epidote, Hbl = hornblende, Hm = hematite, Ill = illite, Ilm = ilmenite, I-S = mixed-layered illite-smectite, Kln = kaolinite, Pl = plagioclase, Py = pyrite, Qz = quartz, Rt = rutile, Sm = smectite, Tmag = titanomagnetite, Ttn = titanite

**Appendix 4: XRD mineral percentage estimates**

A table below shows relative mineral abundances in percentage obtained from 40 XRD scans. The mineral estimates was adapted from a study by Simpson et al., (2019).

AU#	Easting	Northing	Location	Mineral abundances (%)											Total			
				Qz	Adl	Ab	Ill	I-S	Sm	Chl	Kln	Cal	Py	Gp		Pl		
57488	2751631	6414877	Keillors crosscut	20	66		10								4		100	
57491	2751625	6414879	Keillors crosscut	28	16	35	9				11				1		100	
57493	2751618	6414884	Keillors crosscut	25	37	12	2				13				8	3	100	
57495	2751601	6414886	Keillors crosscut	23	7	41	4				22				3		100	
57498	2751583	6414890	Keillors crosscut	25	15	37	3				16		4				100	
57501	2751544	6414902	Keillors crosscut	29	14	33	8				15				1		100	
57504	2751532	6414902	Keillors crosscut	19	32	14	5				24				6		100	
57507	2751513	6414907	Keillors crosscut	11	7	43	5				21		13				100	
57510	2751483	6414911	Keillors crosscut	22	9	48					13		5		3		100	
57515	2751433	6414920	Keillors crosscut	20	6	50	1				16		7				100	
57519	2751393	6414928	Keillors crosscut	22	39	15	5				16				3		100	
57522	2751373	6414927	Keillors crosscut	19	60		4				9				8		100	
57526	2751357	6414933	Keillors crosscut	30	55								15				100	
57531	2750829	6416565	Surface	2						1							97	100
57535	2751125	6416128	Surface	20	2						13		24		1		40	100
57540	2751390	6415735	Surface	30	53		9				3				5		100	
57541	2751395	6415705	Surface	18	65						17						100	
57544	2753030	6415084	Surface	22		65					7		6				100	
57545	2752941	6415115	Surface	33		40		7			10		10				100	
57546	2752853	6415147	Surface	27							7		2				64	100
57547	2752822	6415400	Surface	38						13	10		3				36	100
57548	2752715	6415673	Surface	61			28								11		100	
57551	2752330	6415754	Surface	35		43			10	7		3		2			100	
57554	2751400	6415595	Surface	27							17						56	100
57555	2751519	6415544	Surface	28	48		13				11						100	
57556	2751636	6415555	Surface	44	56												100	
57565	2751984	6416424	Surface	42	51		3								4		100	
57567	2752203	6416463	Surface	32	51		1				13				3		100	
57568	2752287	6416488	Surface	45		28	6				8		13				100	
57569	2752432	6416529	Surface	42		11		15			13		14		5		100	
57573	2752934	6416526	Surface	28				1			10		1				60	100
57574	2750379	6416670	Surface	24							9		3				64	100
57577	2753788	6416450	Surface	20	9					5							66	100
57584	2751827	6414516	Surface	36		16	6	23			10		9				100	
57589	2751392	6415336	Surface	37	52							8			3		100	
57595	2751133	6414706	Surface (rhyolite)	41	56		3										100	
57597	2751375	6415765	Surface	26	49		7				11				7		100	
57598	2751455	6415805	Surface	32	64										4		100	
57601	2751390	6415855	Surface	30	58						10				2		100	
57602	2751369	6415854	Surface	39	58										3		100	

AU# = Sample number

Easting and northing coordinates are New Zealand map grid

**Mineral abbreviations**

Ab = albite, Adl = adularia, Cal = calcite, Chl = chlorite, Gp = gypsum, Ill = illite, I-S = mixed-layered illite-smectite, Kln = kaolinite, Pl = plagioclase, Py = pyrite, Qz = quartz, Sm = smectite

**Appendix 5: Image acquisition log file**

Attached is the measurement log file, which describes camera settings, sample's arrangement during the scanning process, preliminary data observation and preprocessing steps.



BGR\_Measurements\_13nov2019\_logfile.pdf